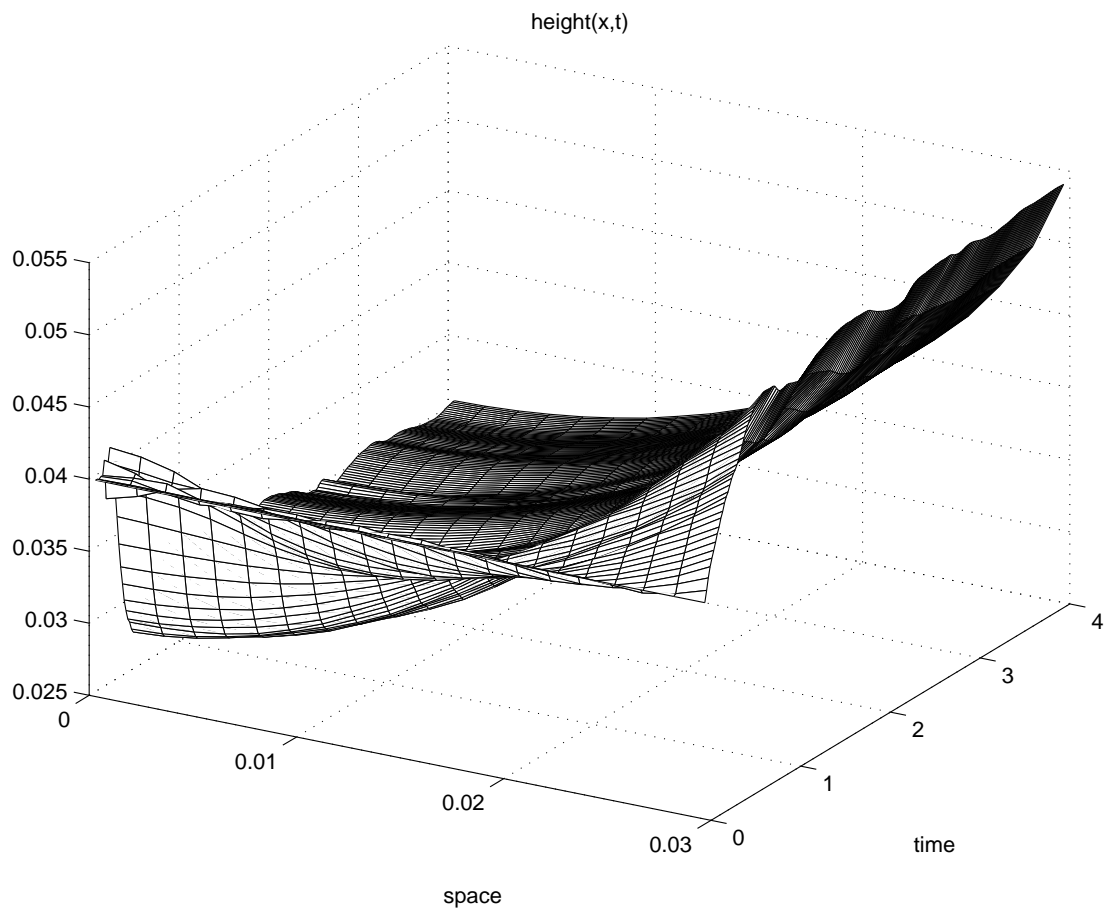




Numerical modelling of the dynamic contact angle

Simon van Mourik



Department of
Mathematics

RUG



Numerical modelling of the dynamic contact angle

Simon van Mourik

Contents

1	Introduction	5
1.1	Outline of this thesis	7
1.2	Goal	7
2	Mathematical Model	9
2.1	Navier-Stokes equations	9
2.2	Boundary conditions	10
2.2.1	Conditions at the wall	10
2.2.2	Conditions at the free surface	10
2.2.3	Contact angle	10
3	Numerical Model	11
3.1	Apertures and VOF-function	11
3.2	Labeling	12
3.2.1	Geometry labels	12
3.2.2	Free-surface labels	13
3.3	Discretized Navier-Stokes equations	14
3.3.1	Time discretization	14
3.3.2	Spatial discretization	15
3.4	Solution method	16
3.4.1	Solution of the discrete Navier-Stokes equations	16
3.4.2	Volume of fluid convection	17
3.5	Conditions at the free surface	18
3.5.1	Condition for the pressure	18
3.5.2	Conditions for the velocity	19
3.6	Conditions at the solid boundary	19
3.7	Contact angle	20
4	Theoretical contact angle models	23
4.1	Introduction	23
4.2	Blake's model	23
4.3	Billingham's model	23
4.4	Velocity profiles	24
5	Empirical models	27

6	Numerical aspects	29
6.1	Stability	29
6.2	The interpolation error of the contact angle	30
6.3	Grid adjustment for gravity	34
6.4	Central discretisation vs. upwind	35
6.5	Billingham vs. static model	37
7	Testing with experiment: theoretical models	43
7.1	Experimental setup	43
7.2	Experiment with M3	44
7.2.1	Static model	45
7.2.2	Blake's model	46
7.3	Contact angle hysteresis	46
7.3.1	Static model with hysteresis	47
7.3.2	Billingham's model with hysteresis	47
7.4	Experiment with Detra	48
7.4.1	Static model	48
7.4.2	Billingham's model	48
7.4.3	Blake's model	49
8	Testing with experiment: empirical models	57
8.1	Experiment with M3	57
8.2	Experiment with Detra	57
8.3	Error percentages	58
9	Implementation methods	63
10	Discussion and recommendations	67
10.1	Practical model	68
10.2	Conclusions and recommendations	71
10.3	Future directions	72
A	Physics of Blake's model	77
B	Program description	79
B.1	Calling sequence	79
B.2	Subroutines	80
B.3	Common block variables	80
C	The input file	83
D	Output files	87
E	Post-processing using Matlab	88
	Bibliography	91

A theory has only the alternative of being right or wrong. A model has a third possibility: it may be right, but irrelevant.

Manfred Eigen

Chapter 1

Introduction

When a liquid is brought into contact with a solid surface, adhesion of the solid with the liquid and cohesion of the liquid become interacting forces, figure 1. The contact angle is often seen as the result of the balance of these forces. (The influence on this balance of the gas in figure 1 is supposed to be negligible and is therefore neglected in many theories). The contact angle is the angle between the liquid and the solid at the contact line, the location where the liquid surface meets the solid surface. Whence the cohesion and adhesion forces are in equilibrium, the matching contact angle is *static*. Out of equilibrium, the liquid near the solid tends to move towards its equilibrium state. The velocity of the contact line depends monotonically on the deviation of the time-dependent (dynamic) contact angle (DCA) with the static contact angle (SCA).

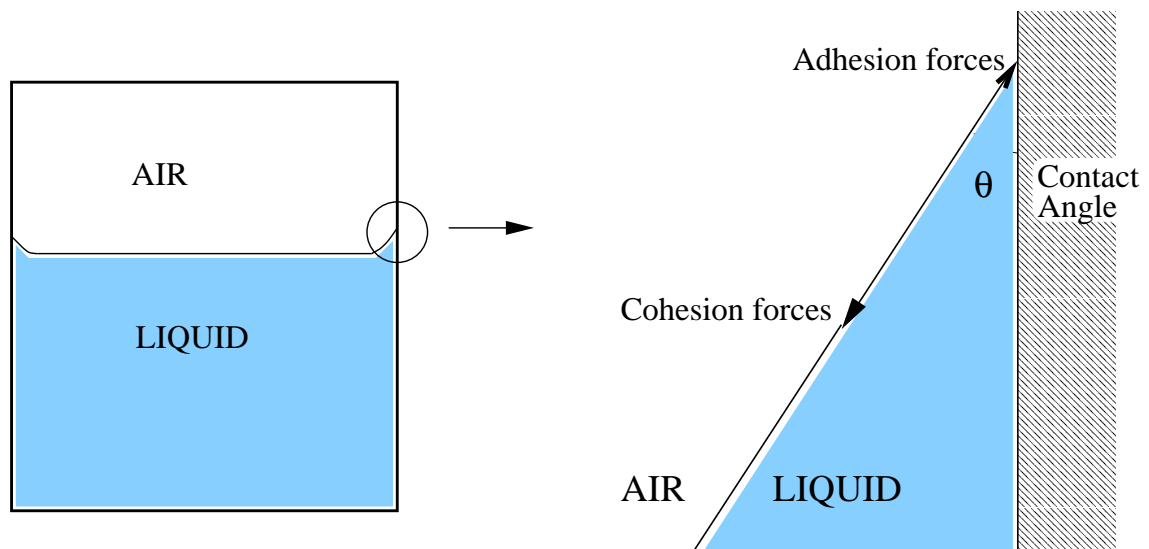


Figure 1.1: *The contact angle represents the balance between surface tension forces and adhesion forces between wall and liquid.*

The DCA plays an important role in fluid dynamics, especially if gravitational forces are not dominant, and surface tension forces are. These situations are represented by a low Bond number (Bo) and a low capillary number (Ca) respectively:

$$Bo = \frac{\rho g R^2}{\sigma} \quad \frac{\text{gravitational forces}}{\text{surface tension forces}} \quad (1.1)$$

$$Ca = \frac{v\mu}{\sigma} \quad \frac{\text{viscous forces}}{\text{surface tension forces}} \quad (1.2)$$

Where ρ , σ , μ , v and R denote the density, surface tension, viscosity, velocity and a characteristic length (tube radius, for example). About the kinetics of the DCA, no satisfying theory has been found yet. Therefore, the numerical modelling of the DCA is often seen as the bottleneck in computational fluid dynamics in which so-called capillary effects play a major role. Many investigations concerning the DCA are empirically based [12]-[19]. Most of the experiments only cover small capillary numbers ($Ca \leq 3 \cdot 10^{-2}$, see chapter 5), so the models based on those experiments are not generally valid. However, at low capillary numbers, the DCA has in general the most influence on the fluid kinetics. Three models that are based on empirical relations are inspected more closely, namely those of Jiang [16], Bracke [17] and Seeberg [18]. The contact line velocity, represented by the capillary number at the boundary, is regarded as a function that depends on the static and dynamic contact angle. The empirical relation is based on minimizing the error between the prediction of the model and experimental results. Experimental data that are often scattered are represented in a general way, but for specific cases these models are not optimized. The scattering in data is of course partially due to error in measurement, but theoretical work suggests that more parameters play an explicit role in the kinetics of the DCA, for example the surface structure of the solid boundary [26]. Attempts have been made from various scientific perspectives to obtain theoretical understanding of the DCA. Fan [20] investigated the kinetics based on the modelling of thermodynamics. Numerous investigations are based on the modelling of hydrodynamics [22]-[24]. Blake [26] based his modelling of the DCA on molecular kinetics, and Billingham [9] based his model on mathematical considerations.

Although it is widely recognised that the DCA can deviate significantly from its static value, the influence of the DCA on the fluid dynamics is not necessarily dominant, for example when gravitational or momentum forces on the liquid are large. When the influence of the DCA is negligible, it is numerically less tedious to impose a static contact angle at the contact line at all times. We refer to this model as the *static model* from now on. Empirical relations are easy to use in general because no parameters have to be fitted for specific fluids. This is preferred when scattering deviations are acceptable.

The computer program (SAVOF96) is based on the incompressible Navier-Stokes equations for simple Newtonian liquids with a free surface. The code uses a VOF method with a Cartesian, staggered grid and computations are done in two dimensions, planar or axisymmetric. Fluid dynamics can be simulated for the general case, i.e. sloshing can be simulated and velocities are not bounded to a maximum value. This means that the models that apply to this code are desired to be valid in the general case also. The code discretises the computational domain into grid cells in which velocity and pressure are calculated locally, i.e. depending only on the state of the neighbouring cells, see section 3. The current (static) contact angle model is also based on a local approach and functions as a boundary condition of the surface at the wall, see section 3. It is desirable if not necessary that the DCA models that are investigated are implemented in a local approach, see also [1].

Theoretically there has been done a lot of work, concerning the DCA. Only few models seem adequate to be implemented in our code and to be investigated numerically, see [1]. These are

the models that are developed theoretically from a perspective that defines the DCA locally, instead of concerning the whole fluid system, like for example Fan [20]. The models by Blake, Jiang, Bracke, Seeberg and Billingham are all suitable for our code and all have different characteristics, positive and negative, as explained in [1]. Investigating the behaviour and characteristics of these models together with the static model should give interesting details about the pro's and con's of these models in various cases.

In this paper, we consider a liquid-filled axisymmetric tube with solid boundary. The behaviour of the contact line height and of the liquid height at the centerline of the tube is monitored after a step reduction of the gravity. The DCA is modelled as a boundary condition of the surface at the wall of the tube. We investigate the validity and accuracy of the theoretical model from Blake [26], Billingham [9] and the static model together with the empirical models of Seeberg, Bracke and Jiang. The accuracy of the models is investigated by means of two experiments with two different liquids; one with a large and one with a small SCA. Experimental results are obtained from the Zarm Institute from the University of Bremen [27]. The computational results are validated by comparison with theoretical velocity profiles.

1.1 Outline of this thesis

The next two chapters will discuss the mathematical model and the numerical code that is used. Thereafter, the theoretical models of Blake and Billingham and the static model, as well as the empirical models of Seeberg, Bracke and Jiang are investigated by means of two experiments. The outcomes of the simulations with the different models, compared to the experimental data, are discussed in chapter 10. Thereafter, a model for practical purposes is proposed.

1.2 Goal

By investigating the behaviour of the different models that are mentioned above, we would like to have answers to the questions:

- Can the accuracy of contact angle models be investigated numerically with our VOF code?
- Which contact angle model is most accurate?
- Is a DCA model preferable to the static model?

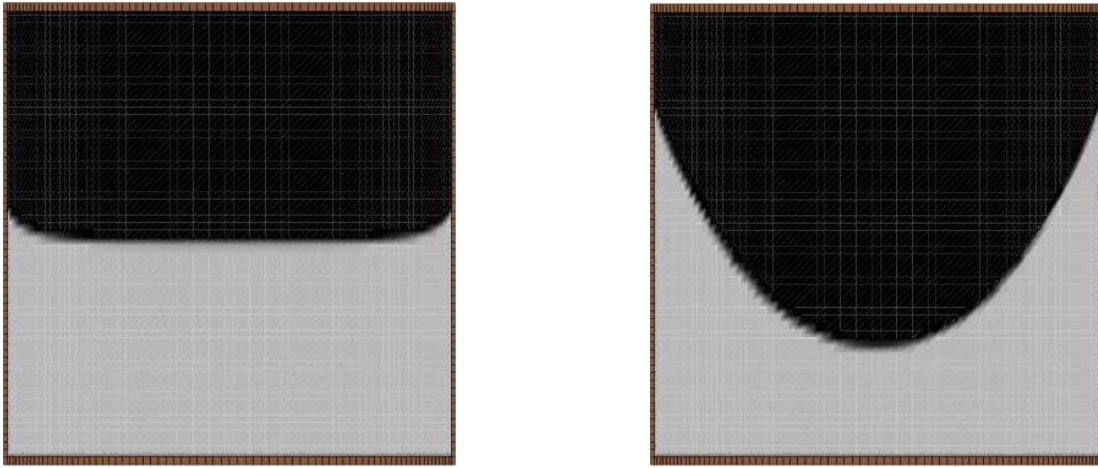


Figure 1.2: *The configuration of the liquid domain. Left: in gravity, the surface is shaped horizontally. At the wall, the surface is curved due to adhesion forces between liquid and wall. The contact angle is the smallest angle between liquid and wall. The gravity is too weak to have influence on the force balance precisely at the wall (the SCA is invariant under gravity), but in the rest of the tube, gravity plays an important role. Right: without gravity, the adhesion forces and the surface tension of the liquid are the only forces working on the liquid. The surface is shaped spherical and the adhesion and surface tension forces are in balance.*

Chapter 2

Mathematical Model

2.1 Navier-Stokes equations

For each fluid in any flow domain the following conservation laws apply: conservation of mass and momentum. Considering an incompressible, Newtonian fluid, we have the following equations in 2D:

- *conservation of mass*

$$\nabla \cdot \mathbf{u} = 0 \quad (2.1)$$

with $\mathbf{u} = (u, v)$ the velocity vector.

- *conservation of momentum*

$$\frac{\partial \mathbf{u}}{\partial t} + \nabla \cdot [\mathbf{u}\mathbf{u}^T] = -\frac{1}{\rho} \nabla p + \nu [\nabla \cdot \nabla] \mathbf{u} + \mathbf{F} + \mathbf{f} \quad (2.2)$$

These are the Navier-Stokes equations. Here, ν is the kinematic viscosity and ρ denotes the density. The pressure is denoted by p and \mathbf{F} stands for external forces (gravity for example). For the axisymmetric case, which we use throughout this thesis, the three-dimensional Navier-Stokes equations are solved, using a transformation $(x, y, z) \rightarrow (r, \phi, z)$. The symbol \mathbf{f} is a virtual body force which originates from the motion of the domain. In this thesis no body force will be used. In general cases this force is given by

$$\mathbf{f} = -\frac{d\mathbf{q}}{dt} - \boldsymbol{\omega} \times [\boldsymbol{\omega} \times \mathbf{r}] - \frac{d\boldsymbol{\omega}}{dt} \times \mathbf{r} - 2\boldsymbol{\omega} \times \mathbf{u},$$

with

- \mathbf{q} the velocity of the origin \mathcal{O} of the Cartesian co-ordinate frame,
- $\boldsymbol{\omega}$ the angular velocity of the domain with respect to the earth-fixed frame, and
- \mathbf{r} the translation vector from the domain frame.

Of course, equations (2.1) and (2.2) require boundary conditions.

2.2 Boundary conditions

2.2.1 Conditions at the wall

There are two boundary conditions at the wall:

$$u_t = 0 \quad (2.3)$$

$$u_n = 0 \quad (2.4)$$

where $u_t = \mathbf{u} \cdot \mathbf{t}$ denotes the velocity tangential to the wall and $u_n = \mathbf{u} \cdot \mathbf{n}$ is the velocity normal to the wall (\mathbf{n} is the normal direction). The first one is the no-slip condition and the second one states that no fluid penetrates the wall.

2.2.2 Conditions at the free surface

At the free surface two types of conditions are required. Firstly, the continuity of both tangential and normal stress is prescribed:

$$-p + 2\mu \frac{\partial u_n}{\partial \mathbf{n}} = -p_0 + 2\sigma H \quad (2.5)$$

$$\mu \left[\frac{\partial u_n}{\partial t} + \frac{\partial u_t}{\partial \mathbf{n}} \right] = 0 \quad (2.6)$$

where μ denotes the dynamic viscosity, p_0 the atmospheric pressure and σ the kinematic surface tension, i.e. surface tension scaled by the density. $2H = \frac{1}{r_1} + \frac{1}{r_2}$ represents the total curvature of the surface with r_1 and r_2 the radii of curvature of the free surface.

Secondly, an equation describing the advection of the surface is needed. This equation is

$$\frac{DG}{Dt} \equiv \frac{\partial G}{\partial t} + \mathbf{u} \cdot \nabla G = 0 \quad (2.7)$$

It states that liquid only (dis)appears through advection. $G(x, y)$ is an indicator function with $G = 1$ if fluid is present at position (x, y) , otherwise $G = 0$.

2.2.3 Contact angle

At the intersection of the liquid with the wall, a condition for the contact angle between the liquid and the wall is prescribed. The contact angle represents the balance between the cohesion forces of the liquid and the adhesion forces between the liquid and the wall. The static model, that is currently in use, states that the contact angle is a constant:

$$\theta(t) = \theta_0 \quad (2.8)$$

Throughout this thesis (chapters 4.1 and 5), various other models that prescribe a dynamic, i.e. time-dependent contact angle are examined.

Chapter 3

Numerical Model

To perform computer simulations of fluid flow, the flow domain is covered by a Cartesian grid. In every cell of the grid that contains fluid, the discretized Navier-Stokes equations will be solved. Therefore we must know which cell contains fluid, which is a boundary or free surface cell and which is an exterior cell. To indicate this the cells will be labeled. In this chapter we will give the details of the numerical model. Sections 3.1- 3.6 are almost literally taken from the master's theses of Theresa Kleefsman [5] and Dirk-Jan Kort [6].

3.1 Apertures and VOF-function

As mentioned above we cover the (arbitrary) flow domain Ω , in two-dimensional space, with a Cartesian grid. The computational cells of the grid are cut by the curved boundary of Ω in a wide variety. Hence cells with different characters originate. This difference in character is incorporated in the numerical method by introducing *apertures* [2].

In the centre of every computational cell a *volume-aperture* F^b is defined which indicates the fraction of the cell-volume that is open to flow. (In SAVOF96, volume apertures only have discrete values $F^b = 0$ for boundary cells and $F^b = 1$ for interior cells. The three-dimensional extension of SAVOF96, ComFlo, works with real values for F^b (so $0 \leq F^b \leq 1$). For the sake of completeness, the version of ComFlo is treated). Analogously we define in the centre of every cell-face an *edge-aperture* A^x (in x -direction) or A^y (in y -direction). We note that edge-apertures contain information that is one dimension lower than the information given by volume-apertures (e.g. two-dimensional edge-apertures indicate the fraction of a cell-*surface* open to flow, which is one-dimensional information). The use of apertures is illustrated in figure 3.1. The apertures F^b , A^x and A^y are used to discretize the Navier-Stokes equations near the boundary and to compute the boundary velocities (see sections 3.4 and 3.6 in [2]).

Since Ω is partially filled with fluid we need additional information to be able to trace the free surface. This is accomplished by introducing one more volume-aperture F^s (also defined in the centre of every cell) better known as a volume of fluid (VOF) function [28]. This (discrete) function indicates the fraction of a computational cell that is occupied by fluid. As a consequence we have $F^s \leq F^b$ throughout the computational grid. An important difference between the volume-aperture F^b and the VOF function F^s is the time-dependency. As F^b can be computed once before the start of the time integration, the VOF function has to be adjusted every single time step. This procedure is explained in section 3.4.2.

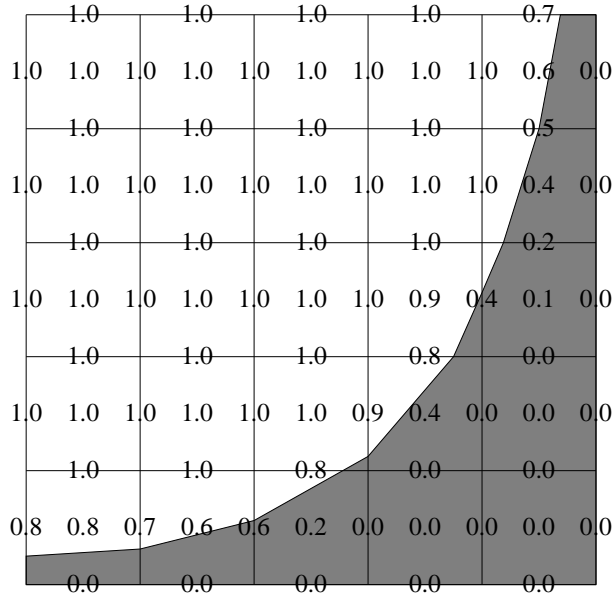


Figure 3.1: *Example of a (discrete) aperture-field (rounded to one decimal place).*

3.2 Labeling

The continuity equation 2.1 and momentum equations 2.2 are discretized on a staggered grid, i.e. the continuity equation is discretized in cell-centres while the velocity components are solved from the momentum equations in the centre of cell-faces.

In section 3.2 of [2] two different methods are examined to apply the boundary conditions. In the first (conventional) method all the boundary velocities (i.e. velocities solved from the solid boundary conditions) were located outside the flow domain, while the second method used some boundary velocities inside the flow domain. The latter turned out to have some advantages compared to the former. For example the second method does not cause stability problems in contrast to the first method. This is the reason why in this report the second method is chosen to set up the numerical model (this method is explained in the section below). Further some new labels are introduced as compared to [2], since the current model includes free-surface flow (section 3.2.2).

3.2.1 Geometry labels

Prior to the time integration the cells are labeled on the basis of the geometry only. First all cells with $F^b \geq \frac{1}{2}$ are labeled as an **F**(low)-cell. This means that at least half of an **F**-cell is open to flow. A computational cell adjacent to an **F**-cell but with $F^b < \frac{1}{2}$ will be called a **B**(oundary)-cell. Finally all the remaining cells are labeled as an **X**()-cell (from exterior). These cells have no significant role in the numerical model.

Based on the cell labeling the velocities are labeled by a combination of two letters; for example a velocity component between an **F**- and a **B**-cell will be called an **FB**-velocity. The geometry labels are illustrated in figure 3.2.

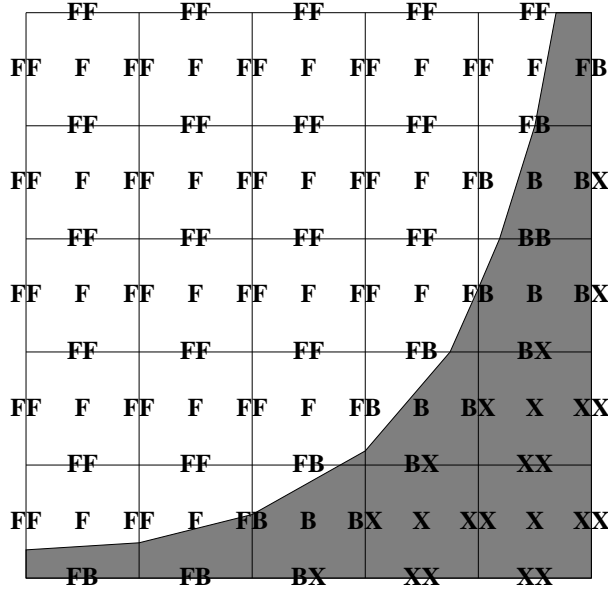


Figure 3.2: *Cell and velocity labels based on geometry only.*

3.2.2 Free-surface labels

The geometry labels are the basis of a more comprehensive labeling to be able to trace the free surface. Since the **B**- and **X**-cells consist of more than 50% solid boundary these labels remain unchanged during the rest of the computational process. Thus, every time step, only the **F**-cells have to be examined on the occurrence of liquid. If a cell contains no fluid, i.e. $F^s = 0$, then the cell is called an **E**(mpty)-cell. All the cells adjacent to an **E**-cell with $F^s > 0$ are labeled as an **S**(urface)-cell.¹ The remaining **F**(low)-cells now will be called **F**(luid)-cells. Figure 3.3 illustrates the free-surface labels in combination with the geometry labels.

Based on the cell labels we decide the following:

- In **E**-, **B**- and **X**-cells no pressure is computed or prescribed since these cells contain (almost) no fluid.
- At the free surface, the pressure is equal to the atmospheric pressure according to the free surface condition 2.6. Then the pressure in **S**-cells is calculated by inter- or extrapolating the atmospheric pressure at the free surface and the pressure in an adjacent **F**-cell.
- In all the **F**-cells the pressure is solved from the continuity equation 2.1 or to be more precise from the pressure Poisson equation (see section 3.4).

The velocities are labeled by a combination of two letters as in the previous section. A priori 15 different combinations can be made. However an **X**-cell can not be adjacent to an **F**-, **S**- or **E**-cell and an **F**-cell can not be next to an **E**-cell. Further **BX**- and **XX**-velocities are ignored since these are not needed in the finite-difference formulas representing the first- and second-order derivatives in the Navier-Stokes equations. Thus only the following 9 combinations remain for further study:

¹In the computer program a cell is labeled an **E**-cell if $F^s < \varepsilon$, with ε a small constant, to take rounding errors into account. Analogously an **S**-cell satisfies $F^s \geq \varepsilon$.

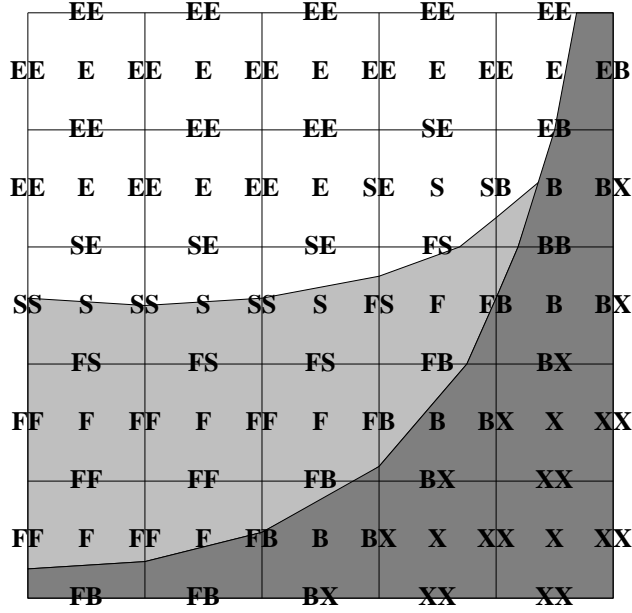


Figure 3.3: *Free-surface labels and geometry labels.*

- **FF**, **FS**, **SS**, **SE** and **EE**. Based on only the geometry these are the **FF**-velocities.
- **FB**, **SB** and **EB**. These are the **FB**-velocities if only the geometry labels are considered.
- **BB**.

Since in both the **F**-cells and the **S**-cells a pressure is defined a pressure gradient can be computed between two **F**-cells, between an **F**- and an **S**-cell and between two **S**-cells. Hence all the **FF**-, **FS**- and **SS**-velocities are solved from the momentum equations. In the remainder of this report we will call these velocities *momentum velocities*. We will call the **SE**- and **EE**-velocities *free-surface velocities* and deal with these in section 3.5.2. The rest of the velocities (**FB**, **SB**, **EB** and **BB**) are the *boundary velocities* and will be discussed in section 3.6.

3.3 Discretized Navier-Stokes equations

In this section we will discuss the discretization of conservation of mass (2.1) and conservation of momentum (2.2).

3.3.1 Time discretization

In [2] has been shown that the labeling method as discussed in the previous section does not cause stability problems. Hence the Navier-Stokes equations are discretized explicit in time. If we use the most elementary time integration method *forward Euler* we get:

$$\operatorname{div} \mathbf{u}^{n+1} = 0, \quad (3.1)$$

$$\frac{\mathbf{u}^{n+1} - \mathbf{u}^n}{\delta t} + \operatorname{grad} p^{n+1} = \nu \operatorname{div} \operatorname{grad} \mathbf{u}^n - \operatorname{div} \left(\mathbf{u}^n \mathbf{u}^{nT} \right) + \mathbf{F}^n + \mathbf{f}^n, \quad (3.2)$$

where δt is the time step, \mathbf{u}^n the velocity field at time $t_n = n \cdot \delta t$ and p^{n+1} the pressure distribution at time t_{n+1} . The pressure gradient is discretized at the ‘new’ time level to ensure that the ‘new’ velocity field from 3.2 is divergence-free.

3.3.2 Spatial discretization

The time-discretized equations 3.1 and 3.2 have to be discretized in space as well. This procedure is exactly the same as in [2]. Hence we only give here the main features of the spatial discretization.

For the spatial discretization conservation cells are used. In these cells both conservation of mass and momentum is required. The conservation cell for the continuity equation is identical to a computational cell, while a conservation cell for the momentum equations consists of two computational cells (see figures 3.4 and 3.5 respectively). Since the continuity equation

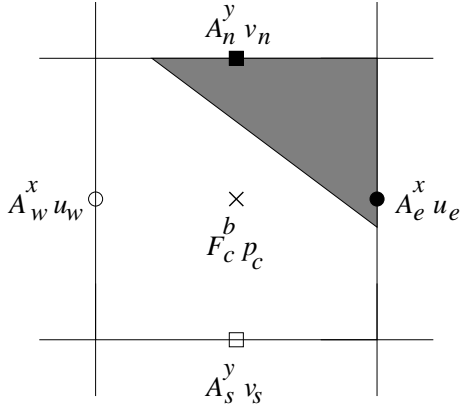


Figure 3.4: Conservation cell for the continuity equation.

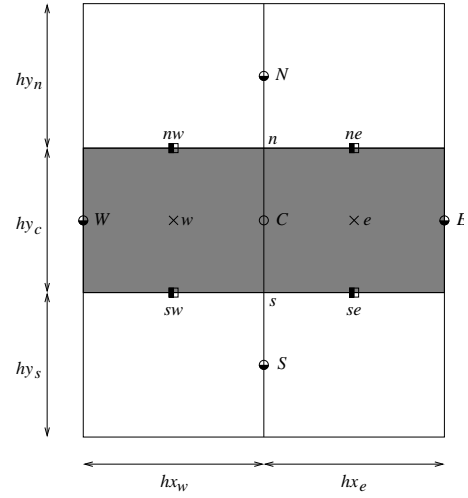


Figure 3.5: Conservation cell for the momentum equation in x -direction.

expresses that the net amount of mass flowing through the boundary of a computational cell must be equal to zero the continuity equation is discretized based on apertures. This way we take into account that no mass can flow through the solid boundary.

The same applies to the convective terms of the momentum equations. These indicate the increase of momentum in a conservation cell because of transport of momentum through the boundary of that cell. Since momentum cannot flow through $\partial\Omega$ the convective terms are discretized based on apertures too. The diffusive terms, the pressure gradient and the body forces indicate the increase of momentum due to stresses rather than transport. Hence these terms in the momentum equations are *not* discretized with apertures.

The above-mentioned results in the following discretized Navier-Stokes equations:

$$D_h^a \mathbf{u}^{n+1} = 0, \quad (3.3)$$

$$\frac{\mathbf{u}^{n+1} - \mathbf{u}^n}{\delta t} + G_h p^{n+1} = \nu D_h G_h \mathbf{u}^n - D_h^a (\mathbf{u}^n \mathbf{u}^{nT}) + \mathbf{F}^n + \mathbf{f}^n. \quad (3.4)$$

Here D_h and G_h are the discrete versions of the divergence and gradient operators. D_h^a indicates that the divergence operator is discretized with apertures. The solution of equations 3.3 and 3.4 is discussed in section 3.4.

3.4 Solution method

In this section we will show how the discrete Navier-Stokes equations are solved and which algorithm is used to ‘move’ the fluid. First some notation is introduced. The set of points in the computational grid where a momentum velocity (**FF**, **FS** and **SS**) is defined will be denoted by Ω_h^f (roughly spoken the points inside the fluid). Further Ω_h^s contains the free-surface velocities (**SE** and **EE**) and Ω_h^b contains the boundary velocities (**FB**, **SB**, **EB** and **BB**). Finally we define $\Omega_h = \Omega_h^f \cup \Omega_h^s \cup \Omega_h^b$ as the entire computational grid (see figure 3.6). We note that the sets Ω_h^f and Ω_h^s vary in time whereas Ω_h^b is time-independent.

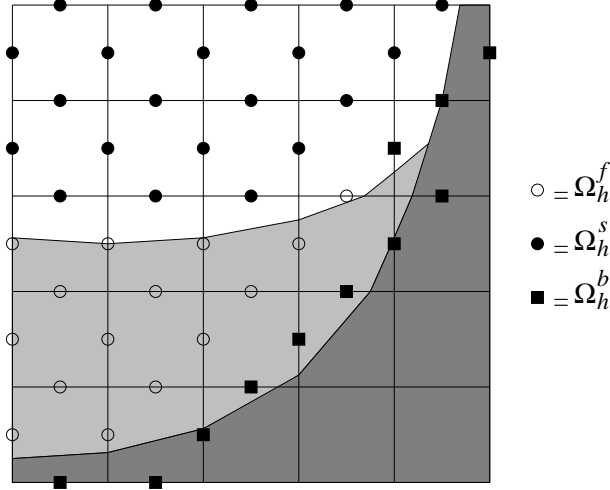


Figure 3.6: *Momentum, free-surface and boundary velocities.*

3.4.1 Solution of the discrete Navier-Stokes equations

We assume an initial velocity field \mathbf{u}^n is given on Ω_h (for $n = 0$ we simply take $\mathbf{u}^0 = 0$). Our goal is to compute a new velocity field \mathbf{u}^{n+1} and a new pressure distribution p^{n+1} from the discrete Navier-Stokes equations 3.3 and 3.4.

First in all the **S**-cells the pressure is set equal to the atmospheric pressure

$$p = p_0 \text{ in } \mathbf{S}\text{-cells,}$$

and a temporary vector field $\tilde{\mathbf{u}}$ is created on Ω_h^f by integrating the momentum equations 3.4 without the pressure gradient, i.e.

$$\tilde{\mathbf{u}} = \mathbf{u}^n + \delta t \left\{ \nu D_h G_h \mathbf{u}^n - D_h^a \left(\mathbf{u}^n \mathbf{u}^{nT} \right) + \mathbf{F}^n + \mathbf{f}^n \right\} \text{ on } \Omega_h^f. \quad (3.5)$$

Note that $\tilde{\mathbf{u}}$ is *not* a velocity field. At this stage \mathbf{u}^{n+1} on Ω_h^f and p^{n+1} in all the **F**-cells have to be solved from

$$D_h^a \mathbf{u}^{n+1} = 0 \text{ in } \mathbf{F}\text{-cells}, \quad (3.6)$$

$$\mathbf{u}^{n+1} + \delta t G_h p^{n+1} = \tilde{\mathbf{u}} \text{ on } \Omega_h^f. \quad (3.7)$$

The operator D_h^a works on unknown velocities in Ω_h^f and Ω_h^b , i.e. on momentum and boundary velocities. Hence 3.7 cannot be substituted directly into 3.6 since then the pressure in **B**-cells would be needed; remember that the continuity equation is discretized in **F**-cells while **FB**-velocities are not solved from the momentum equations [4]. This problem does not occur at the free surface because **FS**-velocities are solved from the momentum equations. To avoid this problem of the missing boundary condition for the pressure we write

$$D_h^a = D_h^{a,f} + D_h^{a,b},$$

where $D_h^{a,f}$ and $D_h^{a,b}$ operate on velocities in Ω_h^f and Ω_h^b respectively. Yet the problem is not solved because we can not compute the boundary velocities at the new time level since therefore we would need the entire velocity field at the new time level. That is why these velocities are set equal to the boundary velocities at the old time level, i.e. $\mathbf{u}^{n+1} = \mathbf{u}^n$ on Ω_h^b . This procedure causes an error $\mathcal{O}(\delta t)$ which already has been introduced by the time integration method forward Euler. Then it remains to solve

$$D_h^{a,f} \mathbf{u}^{n+1} = -D_h^{a,b} \mathbf{u}^n \text{ in } \mathbf{F}\text{-cells}, \quad (3.8)$$

$$\mathbf{u}^{n+1} + \delta t G_h p^{n+1} = \tilde{\mathbf{u}} \text{ on } \Omega_h^f. \quad (3.9)$$

Now it is possible to substitute 3.9 into 3.8 resulting in the *pressure Poisson equation*

$$D_h^{a,f} G_h p^{n+1} = \frac{1}{\delta t} \left[D_h^{a,b} \mathbf{u}^n + D_h^{a,f} \tilde{\mathbf{u}} \right] \text{ in } \mathbf{F}\text{-cells}, \quad (3.10)$$

which has to be solved in every **F**-cell in order to produce a new pressure distribution p^{n+1} . The solution of 3.10 is then used to compute the new momentum velocities

$$u^{n+1} = \tilde{\mathbf{u}} - \delta t G_h p^{n+1} \text{ on } \Omega_h^f. \quad (3.11)$$

Finally the free-surface velocities and boundary velocities are adjusted (this has been explained in sections 3.5.2 and 3.6) such that the new velocity field u^{n+1} has been computed on the entire grid Ω_h .

3.4.2 Volume of fluid convection

Once a new velocity field has been computed the position of the fluid has to be changed based on this velocity field. Hereto the donor-acceptor method [28] has been implemented and slightly adjusted to account for the complex geometries.

In the current labeling method fluid can flow from an **F**- or **S**-cell towards an **F**-, **S**- or **E**-cell. Hence at every cell-face with label **FF**, **FS**, **SS** or **SE** a flux is computed indicating the amount of fluid flowing from the donor to the acceptor cell during one time step. Hereby the following considerations have to be made:

- Fluid cannot flow out of an **E**-cell since it is empty ($F^s = 0$).

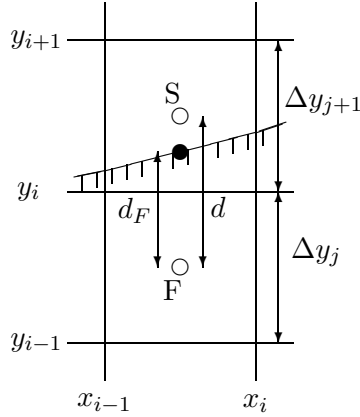


Figure 3.7: A situation for the determination of the surface pressure.

- No more fluid can flow out of the donor cell than the donor cell contains. So the maximum amount of fluid that can be transported is $F^s h_x h_y h_z$.
- An acceptor cell cannot accept more fluid than the void volume in the acceptor cell, i.e. $[F^b - F^s] h_x h_y h_z$.
- The edge-apertures are used for computing the fluxes because part of the cell-face may be solid boundary. Of course through this part of the cell-face no fluid can flow.
- Due to rounding errors F^s can become less than zero or greater than F^b . Hereto these values of F^s are reset at the end of the volume of fluid convection.

After the volume of fluid convection the cells and velocities are relabeled based on the new volume of fluid distribution. At this stage one time cycle has been completed and the entire process is repeated until the maximum simulation time has been reached.

3.5 Conditions at the free surface

3.5.1 Condition for the pressure

The curvature of the surface, needed to apply condition 2.6, is also calculated with the indicator function. Application of condition 2.6 gives thereafter a value p_{fs} for the pressure at the free surface. At each position, a block of 3×3 cells is considered for interpolation. Linear interpolation of this pressure between the corresponding surface cell and full cell gives then a relation which is added to the system describing the discrete Poisson equation for the surface cell. Now an example of this procedure will be given.

See figure 3.7. The average height of the surface in the upper cell, the S-cell, is $F_{i,j+1} \Delta y_{j+1}$. The distance from the centre S of the S-cell to the surface is now

$$d_S = \frac{1}{2} \Delta y_{j+1} - F_{i,j+1} \Delta y_{j+1} \quad (3.12)$$

and the distance from the centre F of the lower cell, the F-cell, to the surface is

$$d_F = \frac{1}{2} \Delta y_j + F_{i,j+1} \Delta y_{j+1} \quad (3.13)$$

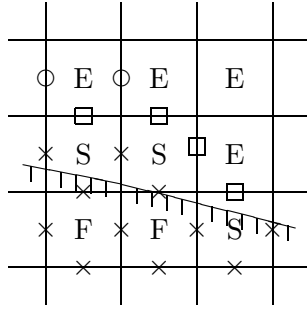


Figure 3.8: A situation at the surface. A \times marks the positions at which a momentum equation is used. The symbols \circ and \square mark positions at which velocities are needed due to the application of a momentum equation in a neighbouring \times -position.

The distance between both cell centra is given by

$$d = \frac{1}{2}\Delta y_j + \frac{1}{2}\Delta y_{j+1} \quad (3.14)$$

The relation for the pressure at the free surface which is added to the system describing the discrete Poisson equation for this surface cell is now given by linear interpolation of the pressures in S and F:

$$p_{fs} = \frac{d_{SP}p_F + d_{FP}p_S}{d} \quad (3.15)$$

Here p_F denotes the pressure at F and p_S the pressure at S.

3.5.2 Conditions for the velocity

In section 3.4.1, it was mentioned that the momentum equations had to be applied at cell faces between full cells and/or surface cells and/or outflow cells. These positions are marked with a \times in Figure 3.8. Section 3.3.2 makes clear that then also velocities have to be defined at the positions marked with a \circ or a \square . A \square -velocity can be obtained by applying $\nabla \cdot \mathbf{u}$ in the neighbouring S-cell. For the situation in the S-cell in the middle, the \square -velocity is obtained by applying $\frac{\partial u}{\partial x} = 0$ and $\frac{\partial v}{\partial y} = 0$. Thereafter the \circ -velocities can be obtained by applying condition 2.6, with x and y instead of \tilde{t} and n , in the corners between the E- and S-cells.

3.6 Conditions at the solid boundary

In boundary cells interpolation and mirror points are used to satisfy the boundary conditions. The case of a vertical wall with fluid at the left will be handled here. See Figure 3.9. The point of definition of the horizontal velocity is at the vertical wall. Therefore it gives no problems:

$$u_{i,j} = 0 \quad (3.16)$$

However, the point of definition of the vertical velocity is half a mesh width away from the boundary. Now a mirror point, defined at a half mesh width outside the solid boundary, will

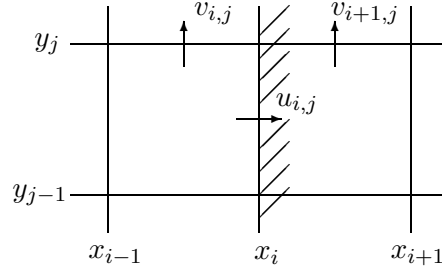


Figure 3.9: A situation at the boundary.

be used. This gives for a no-slip wall

$$v_{i,j} = -v_{i+1,j} \quad (3.17)$$

and for a free slip wall

$$v_{i,j} = v_{i+1,j} \quad (3.18)$$

3.7 Contact angle

As a boundary condition, every time step, after the fluid height is calculated everywhere, the height at the wall is corrected through

$$\frac{h(x_i + 1) - h(x_i)}{\delta x} = \cot \theta_0 \quad (3.19)$$

Figure 6.11. θ_0 denotes the static contact angle. Equation 3.19 states that the angle of the liquid with the wall is always the same. This static model is the current one used in our code. Dynamic models distinguish themselves by a dynamic contact angle. This corresponds with the substitution $\theta_0 \rightarrow \theta(t)$ in equation 3.19. For convenience, the static model is considered here.

By prescribing the virtual fluid height *in* the boundary cell each time step, the pressure and surface curvature near the boundary are adjusted. Later on, this pressure is used to calculate the resulting fluid velocity near the wall. Finally, the VOF-functions of the cells near the wall are adjusted, using the calculated fluid velocity.

Fully written out, the height h_i in column i is determined by the VOF-functions of three cells through

$$h(i) = \sum_j \delta y F(i, j) \quad (3.20)$$

$F(i, j)$ denotes the fill-ratio of cell (i, j) ($0 \leq F \leq 1$). The virtual fluid height in the boundary, column $i + 1$, is extrapolated linearly from $h(i)$, via

$$h(i + 1) = h(i) + \delta x \cot(\theta_0) \quad (3.21)$$

In case the surface is vertically oriented, the vertical fluid height in column j is calculated over three cells, of which the 'bottom' one is a boundary cell.

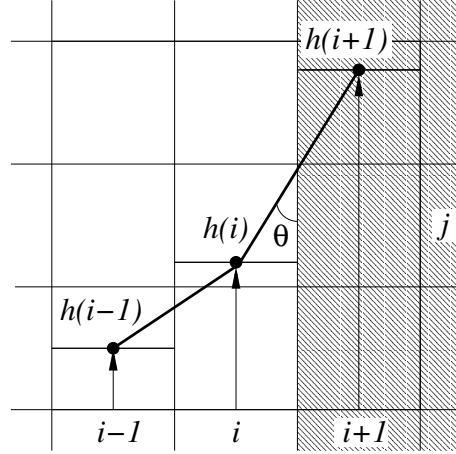


Figure 3.10: Height in column i , defined by fill-ratios. The height in column $i+1$ is extrapolated according to equation 3.21.

$$h(j) = \sum_j \delta y F(i, j) \quad (3.22)$$

The virtual fluid height in column $j + 1$ is extrapolated linearly from $h(j)$, via

$$h(j + 1) = h(j) - \frac{\delta y}{\cot(\theta_0)} \quad (3.23)$$

The resulting discrete heights in columns i and $i + 1$ are used to calculate the curvature of the surface in equation 2.6. The pressure in cell i is calculated and satisfies equation 2.6.

Chapter 4

Theoretical contact angle models

4.1 Introduction

Prescribing a static contact angle (SCA) at all times does not mean that liquid at the boundary will not move. The liquid will move towards its equilibrium position induced by a pressure correction each time step, as explained in 3.7. However, equation 3.19 is not a physically correct one because it assumes a time-independent contact angle, in contrast with, for example, [26].

In this chapter the investigation is aimed at the three theoretical models of Blake, Billingham, and the static model. Among these, Blake is the only one with physical background, see [1]. The static model is introduced in section 2.2.3. We now introduce the models by Blake and Billingham.

4.2 Blake's model

The dynamic contact angle model, as given in [26], is:

$$h_t = 2\kappa_s^0 \lambda \frac{\hbar}{\eta v} \sinh\left(\frac{\gamma[\cos \theta_0 - \cos \theta(t)]}{2nkT}\right) \quad (4.1)$$

With h the contact line height, h_t the contact line velocity (CLV), $\theta(t)$ the dynamic contact angle (DCA), and θ_0 the SCA. The rest of the parameters together with physical derivation is given in appendix A. Note, that this equation is of the form

$$h_t = A \sinh(B[\cos \theta_0 - \cos \theta(t)]) \quad (4.2)$$

4.3 Billingham's model

The model by Billingham [9] is based on mathematical considerations only. This implies a qualitative relation between the CLV and the discrepancy between the SCA and the DCA. This is in agreement with Blake's theoretical model:

$$h_t = \lambda[\cot \theta_0 - \cot \theta(t)] \quad (4.3)$$

Here λ (m/s) is an undefined parameter, thus to be fit by experiment. Furthermore, we note that

$$\cot \theta = \frac{h_w - h_i}{\frac{1}{2}\delta x} = h_x \quad (4.4)$$

(see figure 6.11).

4.4 Velocity profiles

The models of Blake and Billingham contain parameters that can be regarded as numerical coefficients that can be fit by experiment. Blake's model has physical background, and therefore we suppose that Blake's velocity profile has a correct physical behaviour.

The difference between Blake's and Billingham's model is now illustrated by some plots of the contact line velocity as a function of θ_0 and $\theta(t)$. The parameters (λ , A and B) are set to unity. Figures 4.1 and 4.2 show the contact line velocity as a function of $\theta(t)$ and θ_0 . Figure 7.4.2 shows it as a function of $\theta(t)$, with $\theta_0 = 5.5^\circ$. The first two figures show the vast difference in range and the third one emphasizes the different behaviour of both, especially with small θ_0 . In formula:

$$\sup_{\theta_0 \rightarrow 0} |\cot \theta_0 - \cot \theta(t)| = \infty \quad (4.5)$$

$$\sup_{\theta_0 \rightarrow 0} |\sinh(\cos \theta_0 - \cos \theta(t))| = \sinh(1) \quad (4.6)$$

This means in the first place, that with Billingham's model values of $\theta_0 \rightarrow 0$ lead to unrealistic velocity profiles, compared to Blake's model. Another shortcoming of Billingham's model is that $\cot \theta(t) \rightarrow \infty$ for $\theta(t) \rightarrow 90^\circ$.

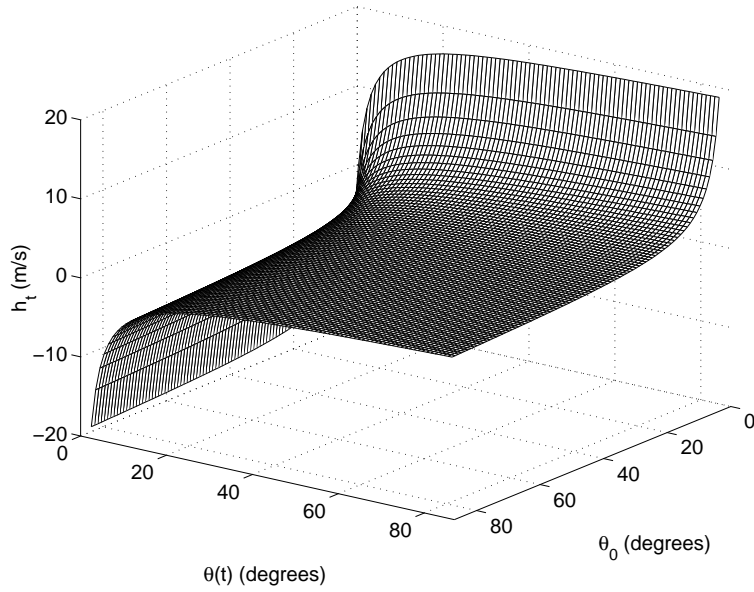


Figure 4.1: The function $h_t = \cot \theta_0 - \cot \theta(t)$. The function is unbounded for $\theta_0 = 0$ and has a large range.

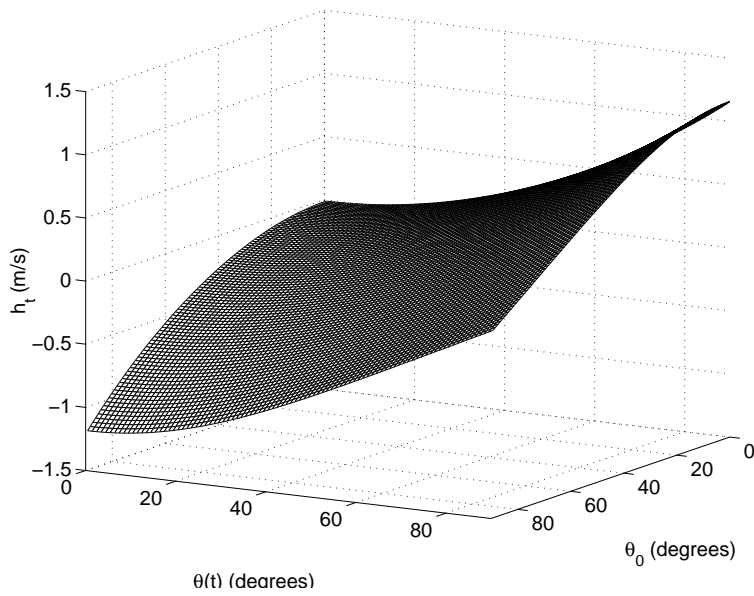


Figure 4.2: The function $h_t = \sinh(\cos(\theta_0) - \cos(\theta(t)))$. This function is bounded and has a relatively small range.

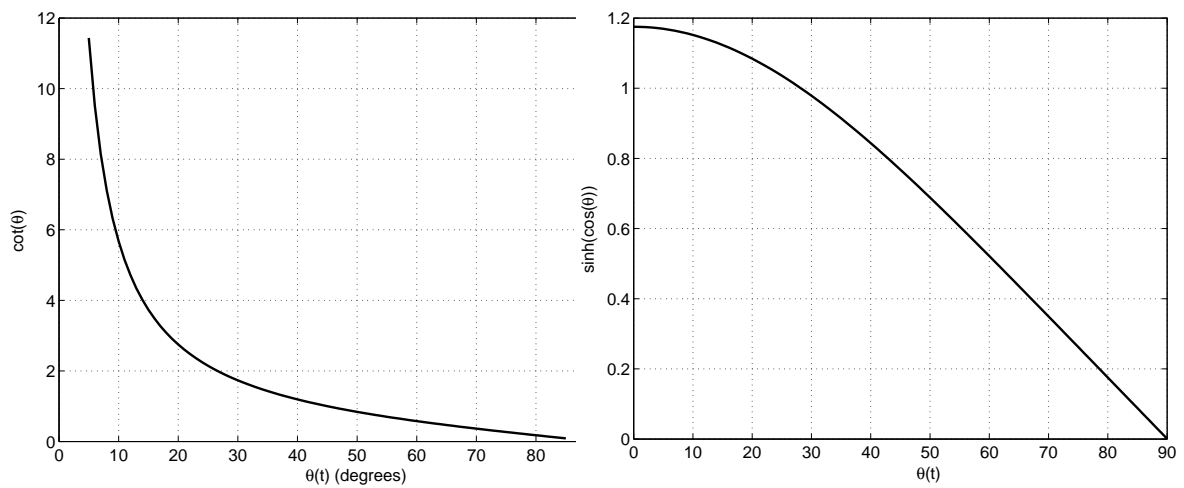


Figure 4.3: $\theta_0 = 5.5^\circ$. *Left: Billingham's model. For contact angles close to the static value, $\cot \theta(t)$, and thus $\cot \theta_0 - \cot \theta(t)$, is a sensitive function of $\theta(t)$. Right: Blake's model. $\sinh \cos \theta(t)$ has a more uniform behaviour.*

Chapter 5

Empirical models

In addition to the three theoretical DCA models, Blake, Billingham and the static one, three empirical DCA models are presented. All are quite similar and based on the fitting of experimental data that correlates the dynamic and the static contact angle with the capillary number $Ca = \frac{\nu h_i}{\sigma}$, with ν the kinematic viscosity and σ the kinematic surface tension. Seeberg shows experimental results that cover a capillary number regime of $0 \leq Ca \leq 3 \cdot 10^{-2}$.

- Jiang's model [16]:

$$\frac{\cos \theta_0 - \cos \theta(t)}{\cos \theta_0 + 1} = \tanh(4.96Ca^{0.702}) \quad (5.1)$$

- Bracke's model [17]:

$$\frac{\cos \theta_0 - \cos \theta(t)}{\cos \theta_0 + 1} = 2Ca^{0.5} \quad (5.2)$$

- Seeberg's model [18]:

$$\frac{\cos \theta_0 - \cos \theta(t)}{\cos \theta_0 + 1} = 2.24Ca^{0.54} \quad (5.3)$$

$$\text{for } Ca \leq 10^{-3} : \quad \frac{\cos \theta_0 - \cos \theta(t)}{\cos \theta_0 + 1} = 4.47Ca^{0.42} \quad (5.4)$$

Compare the $\cos \theta_0 - \cos \theta(t)$ of these models with the $\cot \theta_0 - \cot \theta(t)$ of Billingham, section 4.4. Troubles with unbounded velocities are avoided here. Seeberg compared her model with those of Jiang and Bracke, and found a good agreement for high capillary numbers ($10^{-3} \leq Ca \leq 3 \cdot 10^{-2}$), but not for low capillary numbers. The adjustment of Seeberg's model prescribes lower contact line velocities. Although these models do not have physical background, they might prove useful in certain situations. The data that the models are based on, shows large deviations (scattering) for individual experiments, figures 5.1 and 5.2. The size of those deviations are also shown in the literature ([16], [17] and [18]) and can therefore be taken into account. The small range of capillary numbers for which the models hold is large enough, because for higher numbers the surface tension, and therefore the contact angle, loses its dominance over the fluid kinetics. In all cases only an *advancing* contact line is modelled, which is a huge drawback but not insurmountable. An advantage of these models is, that no parameters have to be fitted anymore; the models are generally valid.

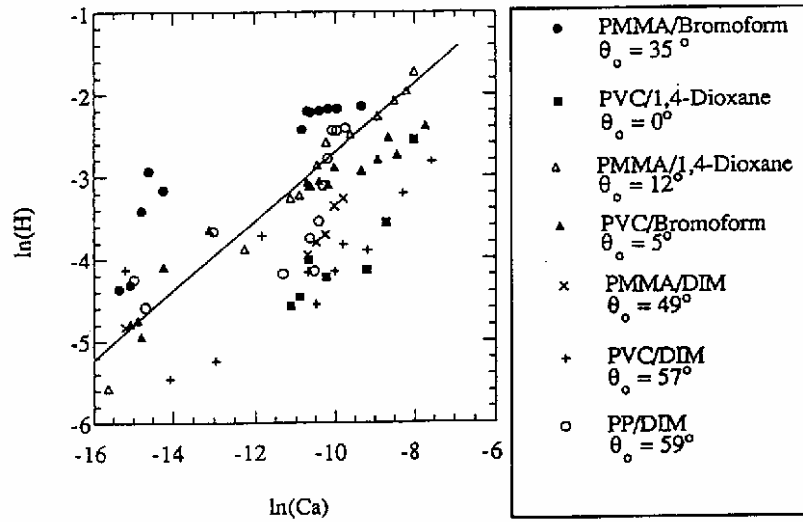


Figure 5.1: Seeberg's model matches experimental data very well for low capillary numbers. The experimental data are widely scattered. H denotes the right-hand side of equation 5.4.

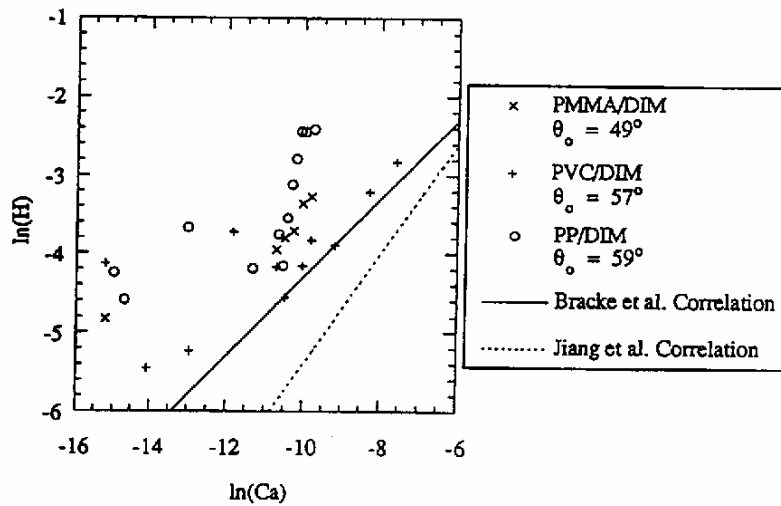


Figure 5.2: Jiang and Bracke do not match experimental data very well for low capillary numbers.

Chapter 6

Numerical aspects

For convenience a uniform grid is assumed throughout this chapter.

6.1 Stability

The stability limit for δt is obtained by Fourier analysis and the substitution $u(x = j, t = n) = c^n e^{ij\theta}$, see [4]. For absolute stability of equation 2.2, it is necessary that errors in u do not amplify during on time-step. The time steps are taken sufficiently small to satisfy this condition, that is

$$\frac{|c^{n+1}|}{|c^n|} \leq 1 \quad (6.1)$$

This is called the CFL-condition. This condition will be taken into account in section 6.4. Furthermore, we have

$$\frac{\sigma \delta t^2}{\delta x^3} \leq \frac{4}{9\pi} \quad (6.2)$$

which guarantees stability of u induced by equation 2.6, see [25]. Here, σ is the kinematic surface tension. For the dynamic models, the behaviour of the variable h_w is not necessarily stable. The stability condition is

$$\left| \frac{\partial h_w^{n+1}}{\partial h_w^n} \right| < 1, \quad (6.3)$$

stating that numerical errors in the contact line height do not amplify during one time step. The static model uses no explicit contact line height h_w , so equations 6.1 and 6.2 suffice. For Billingham's implicit model, equations 6.23 and 6.24, the condition is

$$\left| \frac{\partial h_w^{n+1}}{\partial h_w^n} \right| = \frac{1}{1 + \frac{2\delta t \lambda}{\delta x}} \leq 1 \quad (6.4)$$

This condition is always satisfied. For Billingham's explicit model, equation 6.25, the condition is

$$\left| \frac{\partial h_w^{n+1}}{\partial h_w^n} \right| = \left| 1 - \frac{2\delta t \lambda}{\delta x} \right| \leq 1 \quad (6.5)$$

radius of test tube (m)	R	$1.5 \cdot 10^{-2}$
height of test tube (m)	H	$3.0 \cdot 10^{-2}$
initial fluid height (m)	$h(0)$	$1.48 \cdot 10^{-2}$
kinematic viscosity (m^2/s)	ν	$2.51 \cdot 10^{-6}$
kinematic surface tension (m^3/s^2)	σ	$2.97 \cdot 10^{-5}$
static contact angle	θ_0	5.5°

Figure 6.1: *Properties of the tube and the fluid Detra.*

which is not always satisfied. Blake's model cannot be written in an implicit form like Bingham's, because of the exponentials in the sine hyperbolic. Taking the derivative in equation 4.2 gives

$$\frac{\partial h_w^{n+1}}{\partial h_w^n} = 1 - \delta t A \cosh(B[\cos \theta_0 - \cos \theta(t)]) \frac{\partial \cos \theta(t)}{\partial h_w^n} \quad (6.6)$$

The abbreviation $h_w^n - h_i^{n+1} = \delta h$ leads to

$$\frac{\partial \cos \theta(t)}{\partial h_w^n} = \frac{-\delta h^2}{[\frac{1}{4}\delta x^2 + \delta h^2]^{\frac{3}{2}}} + \frac{1}{\sqrt{\frac{1}{4}\delta x^2 + \delta h^2}} \leq \frac{2}{\delta x} \quad (6.7)$$

Furthermore it is noted that $\cosh(\cos \theta_0 - \cos \theta(t)) \leq \cosh 2$.

Altogether, the general stability condition for Blake's explicit model is

$$\frac{\delta t AB}{\delta x} \cosh(2B) \leq 1 \quad (6.8)$$

6.2 The interpolation error of the contact angle

Consider the following experiment. In an axisymmetric tube with small diameter, the liquid surface is set perfectly horizontal and gravity is set to $g = -9.8 \text{ m/s}^2$. When the liquid has settled itself into equilibrium position, gravity is released to $g = 0.0 \text{ m/s}^2$. The step response of the contact line height is monitored. The liquid settles itself into equilibrium configuration in time. The test fluid is Detra and the properties are given in figure 6.2. Throughout this chapter, Detra is used as a test fluid, on a 40×60 grid.

The DCA is determined by linear interpolation between the height at the wall and the fluid height at $\frac{1}{2}\delta x$ away from the wall, equation 6.24. From figure 6.3 it is seen that at equilibrium, a straight line between h_w and h_i has a greater contact angle with the wall than the curved surface has. This causes a higher contact line velocity, according to formulas 4.2 and 4.3, (figure 6.2) due to the interpolation error. The equilibrium height of the fluid depends also on this error, for the DCA models as well as for the static model. The reasoning is as follows. In absence of gravity the shape of the meniscus of the fluid (at equilibrium) is spherical, see [8].

In equilibrium position ($\theta(t) = \theta_0$) the position of the liquid surface can be described as

$$x^2 + h^2 = r^2 \quad (6.9)$$

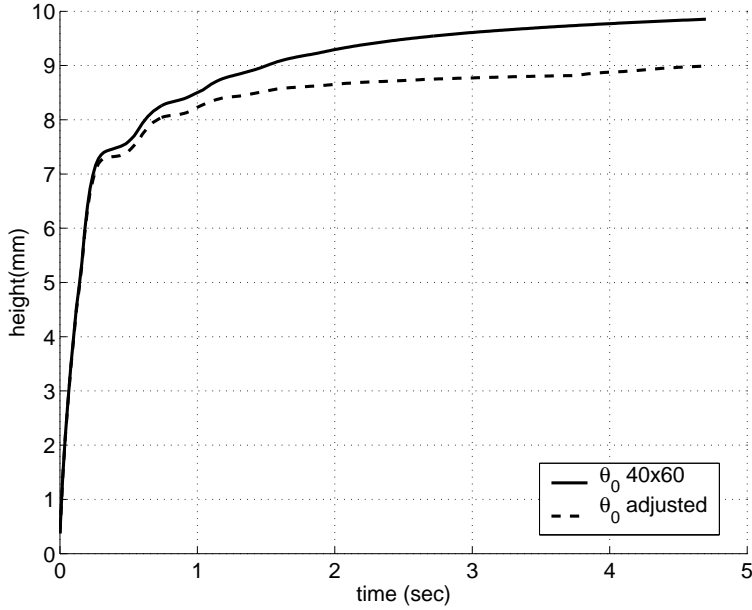


Figure 6.2: Blake's model for Detra. The adjustment of the SCA has a large influence on the equilibrium height of the contact line.

With $-R \leq x \leq R$ the spatial position, h the fluid height, and r the radius of the sphere. In figure 6.3, we assume $0^\circ \leq \theta_0 \leq 90^\circ$. Note that r depends on R and θ_0 . Moreover, the following relation holds

$$\frac{\partial h}{\partial x}|_w = \cot \theta_0 = \frac{R}{\sqrt{r^2 - R^2}} \quad (6.10)$$

The theoretical contact line height is then

$$h_{i+\frac{1}{2}} = h_w = -\sqrt{r^2 - R^2} \quad (6.11)$$

With h_w the contact line height. Suppose the contact line has reached its equilibrium position. The fluid height at h_i is determined as the average height over the cell (see figure 6.11), so

$$h_i = \frac{1}{\delta x} \int_{R-\delta x}^R -\sqrt{r^2 - x^2} dx \quad (6.12)$$

The calculated $\cot \theta(t)$ is

$$\cot \theta_c = 2 \frac{h_w - h_i}{\delta x} \quad (6.13)$$

The error that is made, $\theta_c - \theta_0$, will increase for small θ_0 , because at equilibrium the actual surface is then more curved. Implicitly, the symbolic formula for the error is given above. However, fully written out it has a complicated form which is hard to analyse. Figure 6.3 indicates that the error reduces for finer grids and increases for smaller θ_0 .

At this point a mathematical expression is derived for the differences in contact line equilibrium heights for different grids in figure 6.2. The substitution $\theta_0 \rightarrow \theta_c$ gives the equilibrium

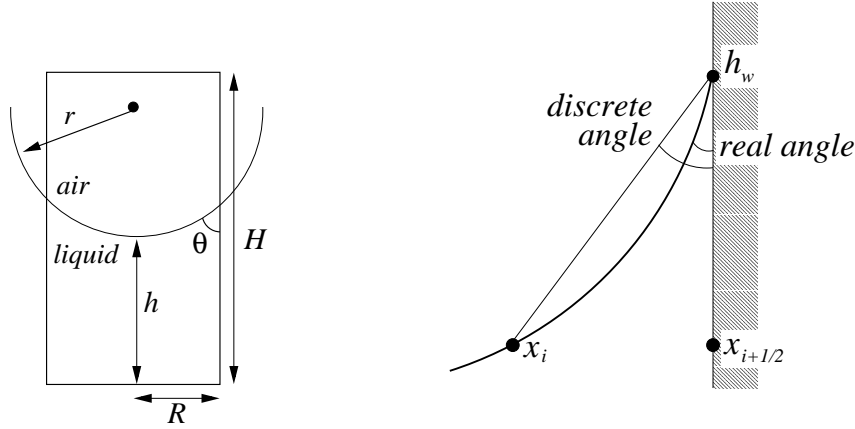


Figure 6.3: In equilibrium the meniscus is shaped spherical and the discrete contact angle is larger than in theory.

height that matches θ_0 . Whence $\theta(t) = \theta_0$, the code calculates $\theta(t) = \theta_c$, which is the SCA, and the contact line stops moving.

The next example hopefully gives an idea of how the error behaves for different grids. Consider an axisymmetrical tube with $R = 1.5 \cdot 10^{-2} \text{ m}$, $\theta_0 = 5.5^\circ$ and 8 grid cells in x-direction. $\cot \theta_0 = 10.39$. By equation 6.10 we find that $r = 1.501 \cdot 10^{-2} \text{ m}$ is only a fraction greater than R . After that, equation 6.9 is solved: $h_{wall} = -1.9 \cdot 10^{-3} \text{ m}$. This is the height with respect to the height of the center of the circle with radius r . Equation 10.9 yields $h_i = -6.2 \cdot 10^{-3} \text{ m}$. Finally 6.13 yields $\cot \theta = 4.31 \rightarrow \theta_c = 13.1^\circ$. Refining the grid a factor 10 to $\delta x = 2 \cdot 10^{-4} \text{ m}$ yields $\cot \theta = 8.16 \rightarrow \theta_c = 7.0^\circ$. Refining to $\delta x = 2 \cdot 10^{-5} \text{ m}$, so at 800 grid cells in x-direction, yields $\cot \theta = 10.04 \rightarrow \theta_c = 5.7^\circ$, which is close to the analytical value.

A validation of the theory is made by adjusting θ_0 as done above. For two different grids, 40×60 and 80×120 cells, the corrected values for θ_c are derived. The values are $\theta_c = 9.35^\circ$ and $\theta_c = 7.78^\circ$ respectively. Figure 6.4 shows the desired results for Blake's model.

Remarkably not only the equilibria show good resemblance but for the whole time interval the CLV's are practically the same. Figure 6.5 shows the results for Billingham's model and the static model respectively. Here, the curves are also similar but resemblance is less than with Blake's model. The equilibrium heights are the same for all models and for all grids.

For a tube of radius $R = 0.02 \text{ m}$ and a fluid with $\theta_0 = 5.5^\circ$, the different θ_c are calculated. From figure 6.6 it is seen that without correcting the static contact angle, a large number of grid cells is needed for an acceptable small error.

Another way of avoiding a large error in determining the contact angle, is to draw a second (or higher) order polynomial through three surface points. The theoretical error in surface height is then reduced from $\mathcal{O}(\delta x^2)$ to $\mathcal{O}(\delta x^3)$.

The surface height in the two cells adjacent to the boundary is represented by the polynomial of the form:

$$h(x) = \alpha x^2 + \beta x + \gamma \quad (6.14)$$

The three surface points are shown in figure 6.11. The height in h_{i-1} and h_i are calculated by VOF-functions. The boundary conditions take into account conservation of mass. This

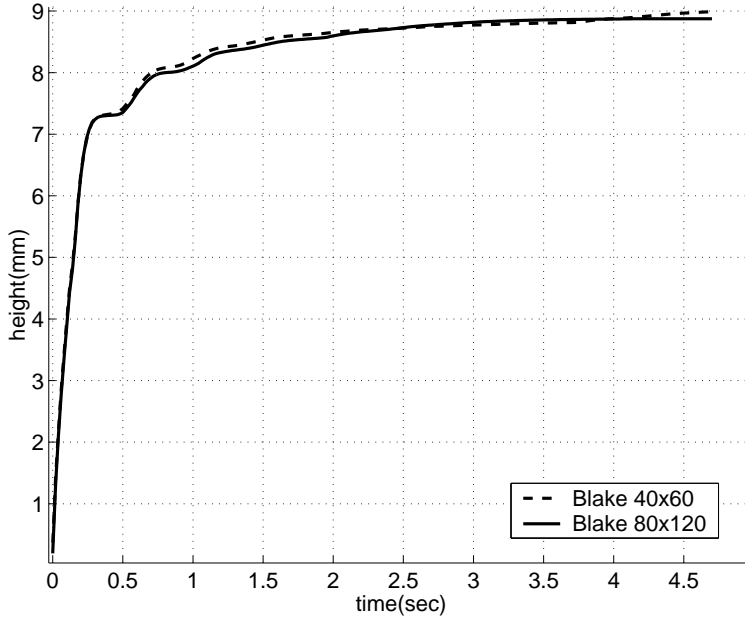


Figure 6.4: *Blake's model. For two different grids the corrected SCA is prescribed. The results are similar for all t .*

means that under the surface, represented by the polynomial, the computed amount of liquid is present.

$$h_i = \frac{1}{\delta x} \int_{x_{i-\frac{1}{2}}}^{x_{i+\frac{1}{2}}} h(x) dx = \sum_j \delta y F(i, j) \quad (6.15)$$

for position i , and analogous for $i-1$. $F(i, j)$ is the computed amount of liquid, and denotes the filling ratio (VOF-function) of cell (i, j) . The contact line height implies the third boundary condition:

$$h(\delta x_{i-1} + \delta x_i) = h_w \quad (6.16)$$

Here, a horizontal orientation of the liquid surface is assumed, which is analogous to a vertical one. Drawbacks of the polynomial are:

- A 3×3 matrix has to be inverted to derive α , β and γ . This takes a lot more capacity than our current linear method. In a 2D axisymmetrical tube with one contact line, only one matrix has to be inverted, which needs a relatively small capacity. However, in 3D one contact line is represented by one contact point per cell. Inverting n matrices for an $n \times n \times n$ grid can give considerable computational costs.
- The polynomial depends for a great deal on h_{i-1} . In theory, the contact angle is a locally defined phenomenon [26]. Even with a refined grid it is desirable to have the contact angle defined as locally as possible.
- For the general case, the polynomial will give the correct surface height throughout the computational domain within order $\mathcal{O}(\delta x^3)$. Currently, the height is determined from

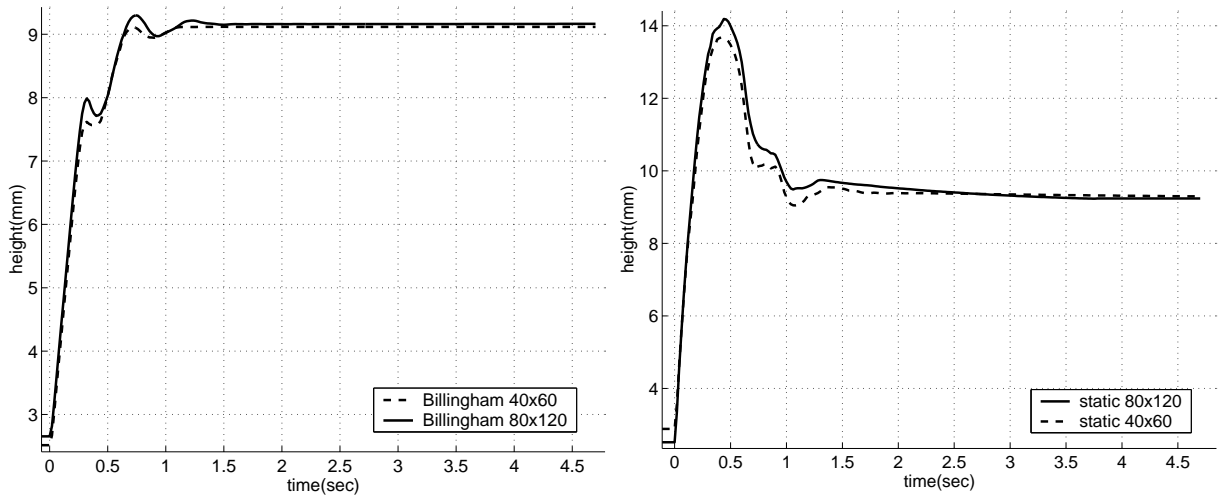


Figure 6.5: *The SCA is adjusted for two different grids. Left: Billingham's model. Right: the static model. The equilibrium heights are the same for all models.*

a linear interpolation of the VOF-function over nine computational cells, three cells in each direction. A second order polynomial can in this case be solved for a horizontal configuration, as well as for a vertical one. For third order one needs to compute over 4×4 cells at a time, and so on. Difficulties may arise if within the 3×3 or 4×4 cells the surface orientation changes. In that case, precision will be lost (height can be double-valued at one position) and the grid has to be refined. For a higher order polynomial, this is more likely to occur.

The polynomial method has not yet been tested. It is however nice to have a second option for the correction of the interpolation error.

6.3 Grid adjustment for gravity

Consider the same experiment as in section 6.2, except this time with gravity. Consider a tube with liquid in equilibrium position under gravity conditions, think of this as a glass of water in rest. In the middle of the tube, the gravity forces are dominant and the surface is flat. At the wall, the adhesion forces are dominant. Especially with a small SCA, the consequence is a sharp surface curvature near the wall. Mathematically: near the wall, the surface height is a highly sensitive function of x . In order to capture the curvature with the computational grid, the grid is locally refined in x -direction. Figure 6.7 shows the influence of local grid refinement. Without refinement, the calculation error of the curvature at the wall, leads to pressure disturbances in equation 2.6 that are so large, that the liquid is constantly put out of its equilibrium position. The equilibrium height of the contact line is always too high, because of the sharp curvature. Application of equation 6.13 reduces that error, but does not take it away. Grid refinement reduces the error further.

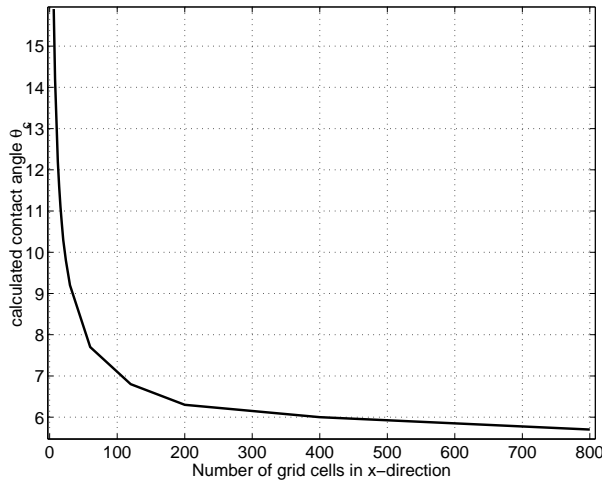


Figure 6.6: *In equilibrium position the meniscus has the same spherical shape for all tube radii. The interpolated contact angle then only depends on the number of (uniform) grid cells in x-direction. The SCA is 5.5° .*

6.4 Central discretisation vs. upwind

In advance of simulating experiments, we would like to know what effect different discretisation methods have on the outcomes. The discretisation of the spatial derivative can be discretised centrally or with upwind, partially or full. The setup of the experiments is described in chapter 7. In order to simplify the analysis, we consider the N-S equations in 1D. The velocity derivative $\frac{\partial u}{\partial x}$ is discretized as follows:

$$\frac{\partial u}{\partial x} = \alpha \frac{u_{i+1} - u_i}{\delta x} + (1 - \alpha) \frac{u_{i+1} - u_{i-1}}{2\delta x} \quad (6.17)$$

Where α is the upwind parameter and $0 \leq \alpha \leq 1$. Here $\alpha = 1$ denotes full upwind and $\alpha = 0$ central discretization. For extra stability, one can choose $\alpha > 0$ but in that case artificial diffusion comes into play.

We will not discuss $\frac{\partial u}{\partial t}$ and $\frac{\partial p}{\partial x}$, knowing that the first one is discretised in time and not spatially, and assuming that $\frac{\partial p}{\partial x}$ is always discretized centrally. The part of the 1D N-S equations that remains is

$$u \frac{\partial u}{\partial x} = \nu \frac{\partial^2 u}{\partial x^2} \quad (6.18)$$

Upwind discretisation of equation 6.18 gives the same result as central discretisation of

$$u \frac{\partial u}{\partial x} = \left[\nu + \alpha \frac{u\delta x}{2} \right] \frac{\partial^2 u}{\partial x^2} \quad (6.19)$$

See also [4]. $\alpha \frac{u\delta x}{2}$ is called artificial diffusion. Of course this is a simplification and even if we know that in both experiments $\nu \sim 10^{-6}$, $\delta x \sim 10^{-4}$ and $u \ll 10^{-2}$ most of the time (meaning relatively small artificial diffusion), the true influence of artificial diffusion has to be checked by simulation. Fourier analysis with the simplified model gives the absolute stability conditions, see [4]:

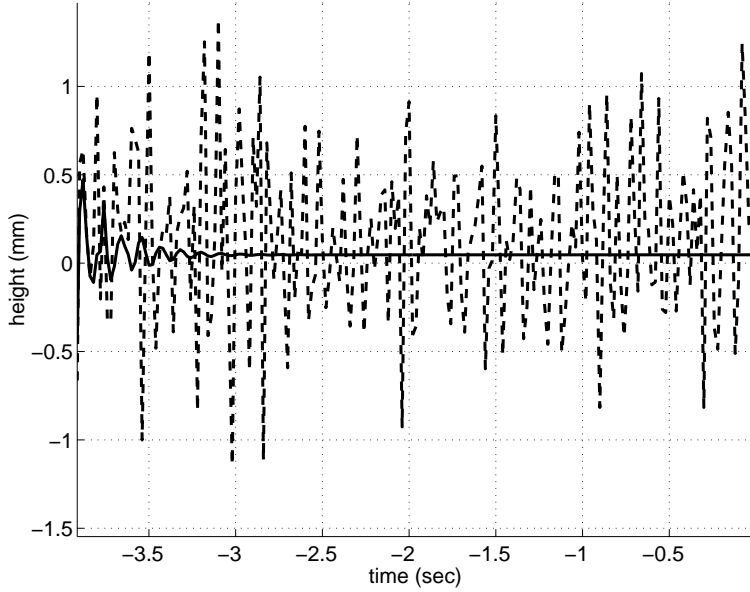


Figure 6.7: *Liquid height at the centerline of the tube. A too coarse grid results in pressure disturbances. Local grid refinement reduces the disturbances.*

$$\delta t \leq \frac{\delta x^2}{2\nu + \alpha u \delta x} \quad \text{and} \quad \delta t \leq \frac{2\nu + \alpha u \delta x}{u^2} \quad (6.20)$$

For our tests, the quantities are of the order of $\delta x \sim 10^{-3} \text{ m}$, $u \sim 10^{-2} \text{ m/s}$ and $\nu \sim 10^{-6} \text{ m}^2/\text{s}$. This means that with $\alpha = 0$ that for the first condition of 6.20 $\delta t \leq 1$ approximately. The second condition requires $\delta t \leq 10^{-2}$ approximately. The CFL-number is defined as

$$CFL = \frac{u \delta t}{\delta x} \quad (6.21)$$

This means that for $\alpha = 0$, $CFL_{max} \leq 10^{-1}$. With $\alpha = 1$, the restrictions of conditions 6.20 are both $\delta t \leq 10^{-1}$, meaning that $CFL_{max} \leq 1$. Upwind discretisation allows a larger time step than central discretisation.

The experiments from chapter 7 are simulated without gravity. At $t = -4 \text{ s}$ the surface is set perfectly horizontal and $g = -9.8 \text{ m/s}^2$. At $t = 0 \text{ s}$, when the liquid has settled into its equilibrium position, gravity is released to $g = 0 \text{ m/s}^2$.

There is another reason for choosing upwind. Central discretisation can give so-called wiggles in case of steep gradients. Figure 6.8 shows the history of the location of the surface for the experiment with Detra, see chapter 7. In little time the surface at the wall (and at the centerline) is elevated from one place to another in a fraction of time, when gravity is released. Consider the simplified 1D N-S equations 6.18. The condition that with central discretisation no wiggles occur, is

$$P \equiv \frac{|u| \delta x}{\nu} \leq 2 \quad (6.22)$$

This gives a restriction on the fineness of the grid, especially when u is large. P is defined as the mesh-Péclet number. Upwind causes no wiggles in the numerical solution of u in equation 6.18. For details, see [4]. Figures 6.4 and 6.4 show that variation of α has negligible influence on the outcomes of the experiments with the liquids Detra and M3.

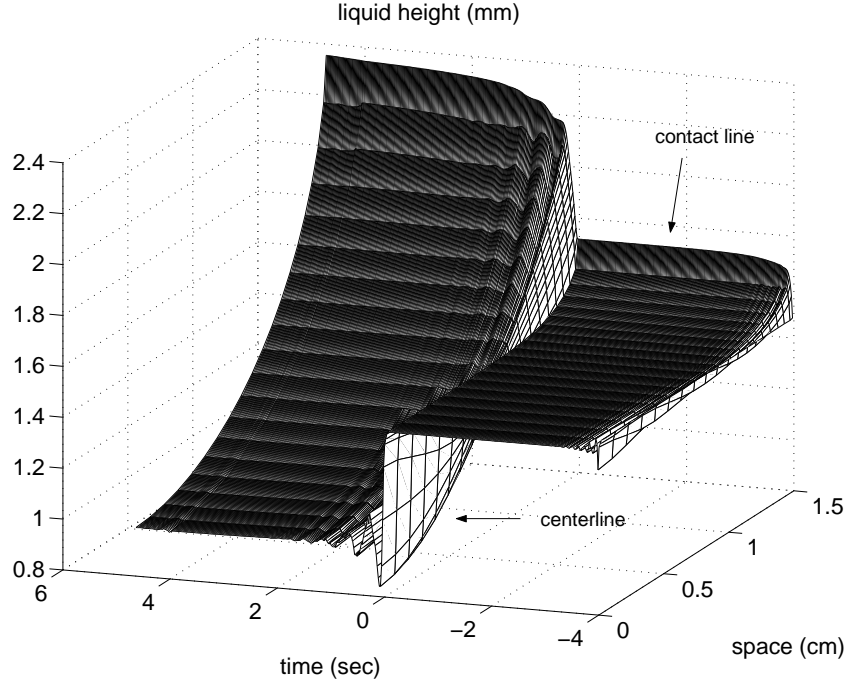


Figure 6.8: At $t = 0$ s gravity is set from $g = -9.8 \text{ m/s}^2$ to $g = 0.0 \text{ m/s}^2$. The liquid surface is set from one equilibrium position into another in little time.

6.5 Billingham vs. static model

Billingham's model can be compared numerically to the static model. Consider $h(x, t)$ as the fluid height. From now on $h(x = x_i, t = n\delta t)$ is noted as h_i^n . Billingham's model is discretised in the following way. The contact angle information is used to update the liquid height along the wall, i.e. h_w^{n+1} the contact line height.

$$h_w^{n+1} - h_w^n = \delta t \lambda (\cot \theta_0 - \cot \theta^{n+1}) \quad (6.23)$$

The contact angle is discretised as

$$\cot \theta^{n+1} = \frac{h_w^{n+1} - h_i^{n+1}}{\frac{1}{2} \delta x} \quad (6.24)$$

This is an *implicit* discretisation, because h_w^{n+1} is on both sides of the equation. Replacing h_w^{n+1} in the right side of the last equation by h_w^n is called *explicit*. (An implicit discretisation is preferable to explicit discretisation, with respect to stability, see chapter 6.1.) So with explicit discretisation, equation 6.23 becomes

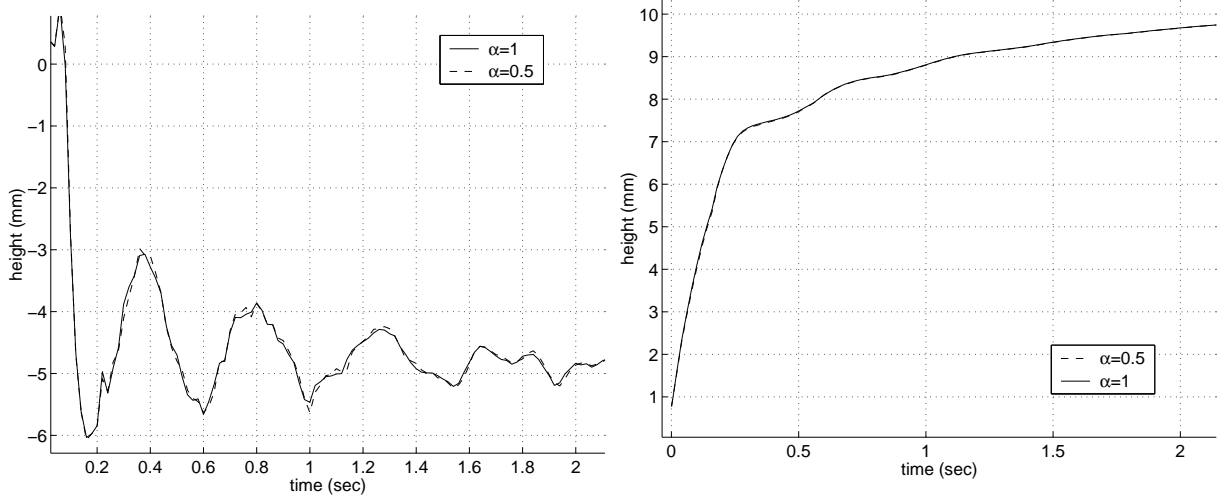


Figure 6.9: *Left: For Detra, variation of α gives has not much influence on the contact line. Blake's model is used. Right: Variation of α has not much influence at the centerline.*

$$h_w^{n+1} - h_w^n = \delta t \lambda \left[\cot \theta_0 - \frac{h_w^n - h_i^{n+1}}{\frac{1}{2} \delta x} \right] \quad (6.25)$$

With the static model, each time step the contact angle is set to the SCA θ_0 . During time-step $n + 1$, the most recent fluid height in the interior that is available is denoted h_i^{n+1} . At the end of time step $n + 1$, the new VOF-functions are calculated and therefore also h_i^{n+2} , etcetera. So during time-step $n + 1$ the virtual height along the wall is adjusted from h_w^n to h_w^{n+1} . The height of the contact line is not explicitly used with the static model, but can be represented by h_w and is adjusted every time the liquid height in the wall ($i + 1$) is adjusted. During time-step n , h_{i+1} is set to (equation 3.21 and figure 6.11):

$$h_{i+1}^n - h_i^n = \delta x \cot \theta_0 \rightarrow h_w^n - h_i^n = \frac{1}{2} \delta x \cot \theta_0 \quad (6.26)$$

At the end of time-step n , the VOF-functions and thus the fluid heights are adjusted to h_i^{n+1} :

$$h_w^n - h_i^{n+1} = \frac{1}{2} \delta x \cot \theta^n \quad (6.27)$$

In the next time-step ($n + 1$), h_w^n is adjusted to

$$h_w^{n+1} - h_i^{n+1} = \frac{1}{2} \delta x \cot \theta_0 \quad (6.28)$$

Subtracting formulas 6.27 and 6.28 gives

$$h_w^{n+1} - h_w^n = \frac{1}{2} \delta x [\cot \theta_0 - \cot \theta^n] \quad (6.29)$$

Where $\cot \theta^n$ satisfies equation 6.27. Billingham's *explicit* model (equation 6.25) with $\lambda = \frac{\delta x}{2 \delta t}$ equals equation 6.29. We summarize the statements above. The static model is time-independent:

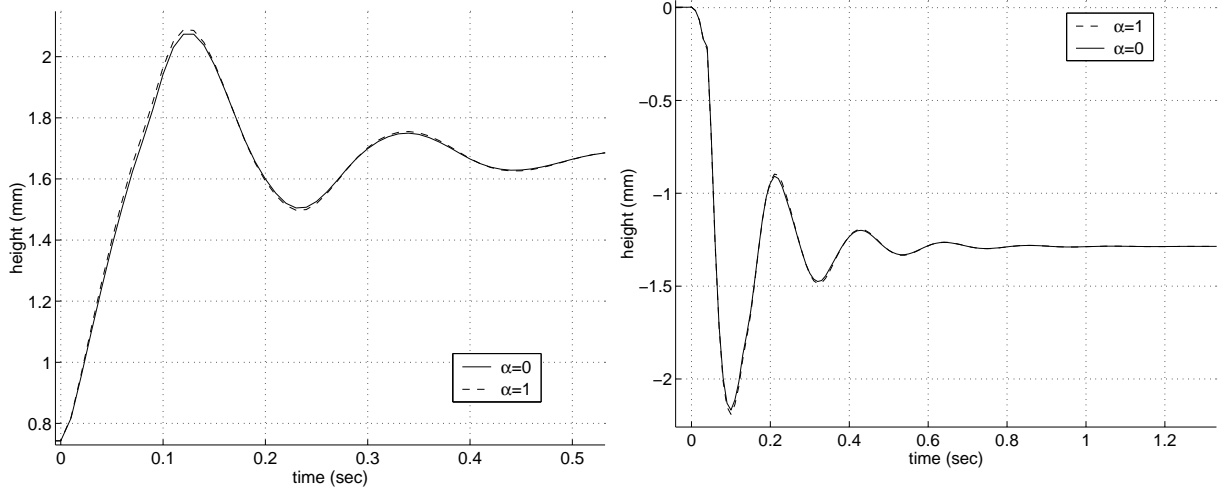


Figure 6.10: *Left: For M3, variation of α gives has no influence at the centerline. Blake's model is used. Right: Variation of α has no influence at the contact line.*

$$h_x = \cot \theta_0 \quad (6.30)$$

and is implemented as

$$\frac{h_w^{n+1} - h_i^{n+1}}{\delta x} = \cot \theta_0 \quad (6.31)$$

Billingham's explicit model is implemented as

$$\frac{h_w^{n+1} - h_w^n}{\delta t} = \lambda \left[\cot \theta_0 - \frac{h_w^n - h_i^{n+1}}{\frac{1}{2}\delta x} \right] \quad (6.32)$$

Choosing $\lambda = \frac{\delta x}{2\delta t}$ in 6.32 yields 6.30 and Billingham explicit equals the static model. Figure 6.12 shows the difference between Billingham's implicit- and the static model.

An explicit implementation of Billingham's model gives in theory a different model than an implicit implementation. The difference is:

$$\text{explicit: } \frac{h_w^{n+1} - h_w^n}{\delta t} = \lambda \left[\cot \theta_0 - \frac{h_w^n - h_i^{n+1}}{\frac{1}{2}\delta x} \right] \quad (6.33)$$

$$\text{implicit: } \frac{h_w^{n+1} - h_w^n}{\delta t} = \lambda \left[\cot \theta_0 - \frac{h_w^{n+1} - h_i^{n+1}}{\frac{1}{2}\delta x} \right] \quad (6.34)$$

Subtracting the two gives a difference of

$$\frac{2\lambda\delta t^2}{\delta x} \left[\frac{h_w^{n+1} - h_w^n}{\delta t} \right] \quad (6.35)$$

Note that $\frac{h_w^{n+1} - h_w^n}{\delta t} \leq u_{max}$. The CFL-condition (see section 6.4) states that

$$\frac{u_{max}\delta t}{\delta x} \leq CFL_{max} \quad (6.36)$$

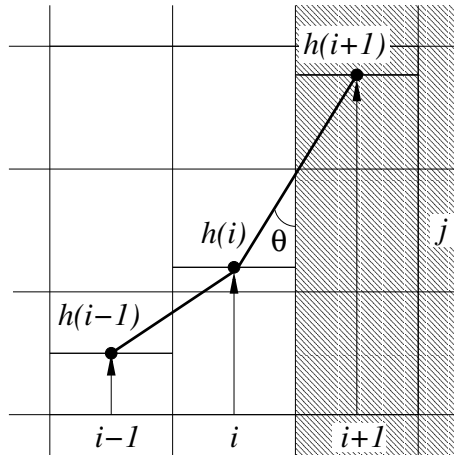


Figure 6.11: *Height defined by fill-ratios.*

with CFL_{max} usually about 1 (with full upwind, see section 6.4). The difference between an implicit and explicit method each time-step is therefore

$$\frac{2\lambda\delta t^2}{\delta x} \left[\frac{h_w^{n+1} - h_w^n}{\delta t} \right] \leq \frac{2\lambda\delta t^2}{\delta x} CFL_{max} \frac{\delta x}{\delta t} = \mathcal{O}(\delta t) \quad (6.37)$$

This difference can be seen as a perturbation, assuming that one of the two methods is the correct one. A finer grid implies a smaller δt by the CFL-condition, reducing the perturbation. Stability for both methods guarantees small perturbations to converge to zero. The stability of both methods is discussed in chapter 6.1. The N-S equations (and therefore h_i) are integrated in time with the forward-Euler method with an error of $\mathcal{O}(\delta t)$. We can conclude that the errors in h_i and in h_w in time behave the same.

In practice, the time step can be taken infinitely small, at considerable computational costs, but not too large, according to stability conditions 6.1 and 6.2. Choosing $\lambda = \frac{\delta x}{2\delta t}$ with Billingham's model gives the same results as the static model. In general, this gives a very large λ . Thus with the static model, we can choose $\delta t = \frac{\delta x}{2\lambda}$ and obtain the same results as with Billingham's model. Unfortunately, the time step is bounded by stability conditions 6.1 and 6.2 and cannot be chosen very large. In other words, Billingham's model can be fit to the static model, but not the other way around.

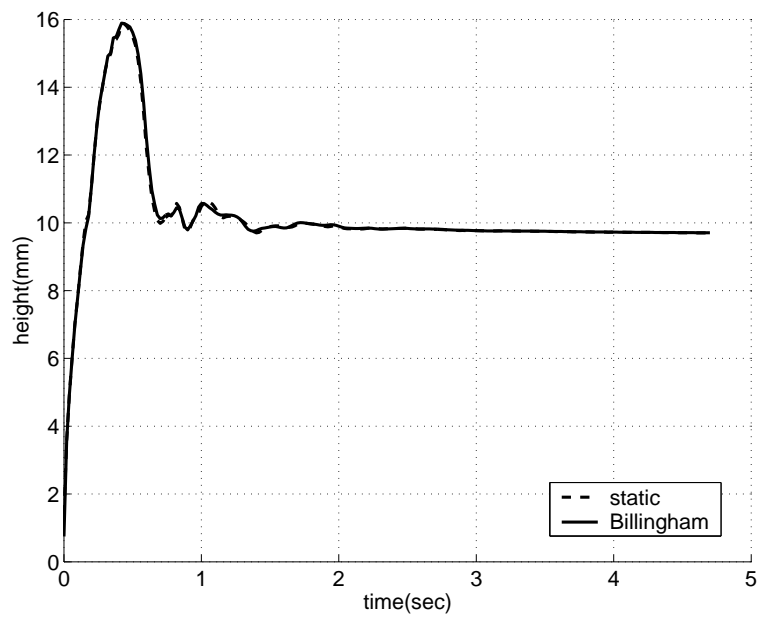


Figure 6.12: *Detra*. Billingham's model gives the same results as the static model for $\lambda = \frac{\delta x}{2\delta t}$. The small difference is perhaps caused by small numerical differences between the explicit and implicit numerical method. A 40×60 grid is used.

Chapter 7

Testing with experiment: theoretical models

7.1 Experimental setup

In an axisymmetric tube with small diameter, gravity is set from $g = -9.8 \text{ m/s}^2$ to $g = 0 \text{ m/s}^2$ at $t = 0 \text{ s}$. The step response of the fluid height at the wall and at the centerline of the tube are monitored. The test is done with two different fluids; one with a small and one with a large SCA. For $t \leq 0 \text{ s}$, the liquid is in equilibrium with its gravity environment. The Bond number is equal to zero after $t = 0 \text{ s}$ and the capillary number is small, because v is small. This means a large influence of the DCA over the liquid kinetics.

$$Bo = \frac{\rho g R^2}{\sigma} \quad \frac{\text{gravitational forces}}{\text{surface tension forces}} \quad (7.1)$$

$$Ca = \frac{v\mu}{\sigma} \quad \frac{\text{viscous forces}}{\text{surface tension forces}} \quad (7.2)$$

R and v are a characteristic length (tube radius) and characteristic velocity (CLV). The Zarm Institute from the University of Bremen simulated this step response by dropping a liquid-filled tube in a special drop tower and registering the liquid movement. Figure 7.1 shows the tower and the capsule that holds the tube and registration equipment.

The test cases that are simulated are described in [27]. For our simulations, we used smaller computational domains as in experiment. This reduces computational costs. Originally, for Detra and M3, $h(0) = 4.8 \cdot 10^{-2} \text{ m}$. We used for Detra $h(0) = 1.48 \cdot 10^{-2} \text{ m}$ and for M3 $h(0) = 4.8 \cdot 10^{-3} \text{ m}$. The smaller liquid domains do not effect the outcomes significantly (figure 7.2). Furthermore, full upwind is applied, which gives the same results as central discretisation for both liquids as seen in chapter 6. The equilibrium configuration for $t \leq 0 \text{ s}$ is also simulated by a step response. At $t = -4 \text{ s}$ the liquid surface is perfectly horizontal and after that the liquid settles itself in equilibrium with the gravity environment. In order to reduce disturbant velocities, the viscosity of the liquid is increased by a factor 10 in gravity. Full upwind is used in all simulations ($\alpha = 1$).

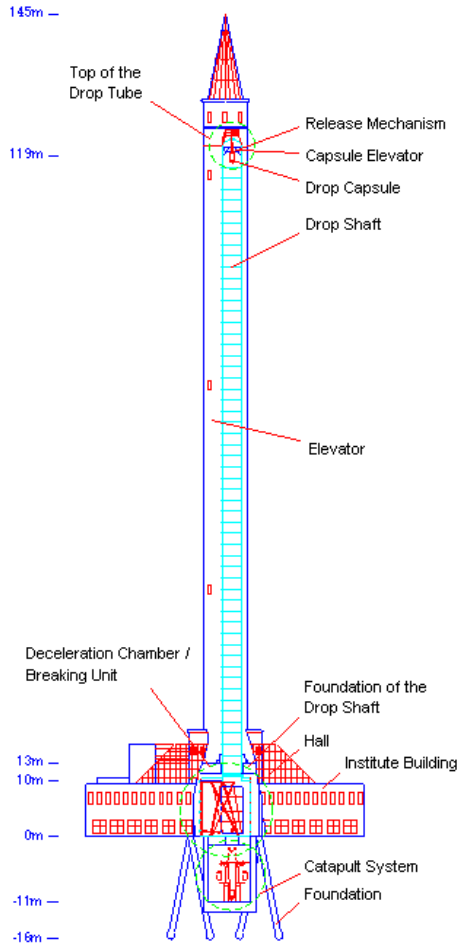


Figure 7.1: *Left: a sketch of the drop tower in Bremen. Right: the capsule that holds the liquid-filled tube and registration equipment.*

	Detra	M3	description
R	$1.5 \cdot 10^{-2}$	$1.0 \cdot 10^{-2}$	radius of test tube (m)
H	$3.0 \cdot 10^{-2}$	$1.0 \cdot 10^{-2}$	height of test tube (m)
$h(0)$	$1.48 \cdot 10^{-2}$	$4.8 \cdot 10^{-3}$	initial liquid height (m)
ν	$2.51 \cdot 10^{-6}$	$2.92 \cdot 10^{-6}$	kinematic viscosity (m^2/s)
σ	$2.97 \cdot 10^{-5}$	$2.06 \cdot 10^{-5}$	kinematic surface tension (m^3/s^2)
θ_0	5.5°	55°	static contact angle
ρ	$9.03 \cdot 10^2$	$8.79 \cdot 10^2$	density (kg/m^3)

7.2 Experiment with M3

M3 has a large SCA ($\theta_0 = 55^\circ$). Near the wall in equilibrium state, the liquid surface is far less curved than with a small SCA. This gives some advantages. The SCA is adjusted, but the difference is small ($\theta_c = 55.3^\circ$). The grid does not have to be refined locally for $t \leq 0$ s. A 40×40 and a 80×80 grid are used.

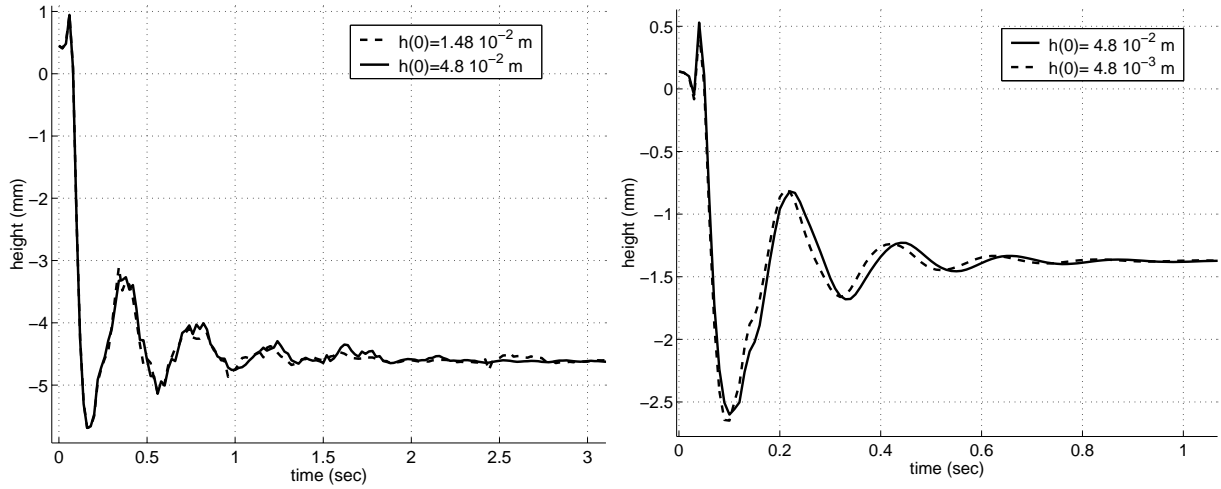


Figure 7.2: Variation of the liquid domain has not much effect on the outcomes of the simulations. Left: the centerline oscillation of Detra. Right: the centerline oscillation of M3.

7.2.1 Static model

The response of the step reduction of gravity of the static model is shown in figure 7.3. The CLV is far too high which causes a large overshoot. As a result, the oscillation at the centerline of the tube does not agree with experiment whatsoever.

Right after $t = 0 \text{ s}$, the contact angle increases after each time step as h_i increases, and is immediately set back to its static value. The dynamic model does not prescribe a SCA, but one that lies closer to it than the current one. Hence, for the static model the change of contact line height per time step is greater than for the dynamic model, resulting in a greater CLV.

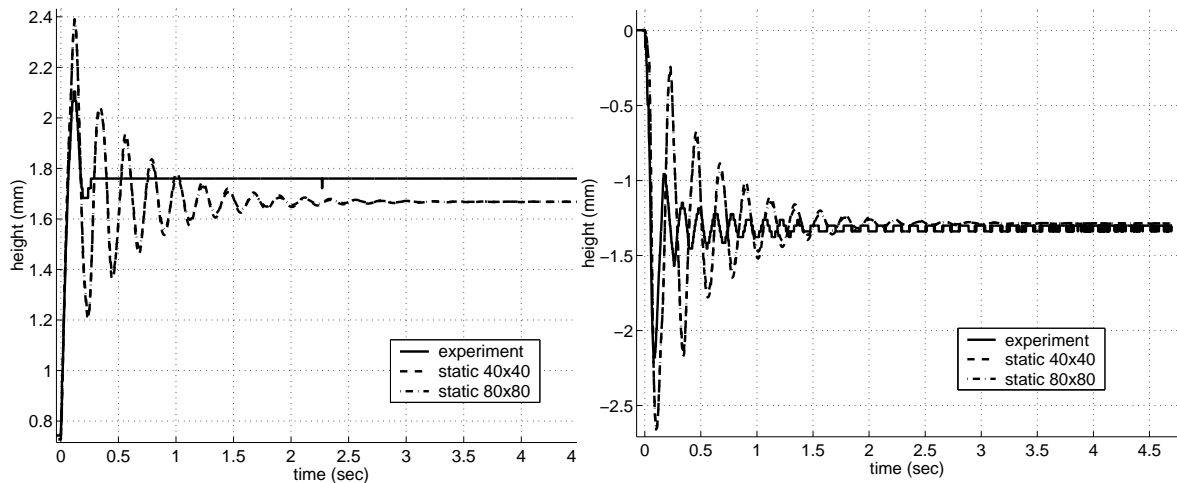


Figure 7.3: M3 with the static model. Left: the CLV is far too high, which causes a large overshoot. As a result, the oscillation in the middle of the tube does not agree with experiment whatsoever (right).

7.2.2 Blake's model

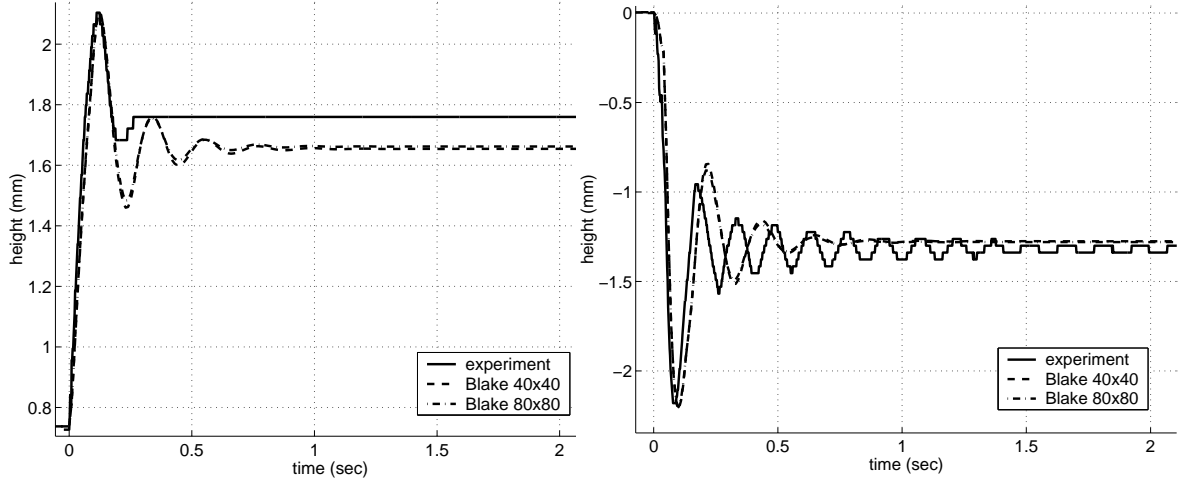


Figure 7.4: *M3 with Blake's model. Left: the contact line oscillates for too long afterwards. This causes capillary forces that counteract the oscillation at the centerline of the tube, which in turns causes large damping of that oscillation (right). The equilibrium height is too low at the wall and thus too high in the middle.*

For Blake's model the parameters A and B are estimated according to [26]. M3 is a silicone oil, so we estimate the parameters of Blake's model according to the silicone oils that are examined in Blake's paper. This gives, in equation 4.2, $\kappa_s^0 = 1.7 \cdot 10^{11} \text{ s}^{-1}$, $\lambda = 0.8 \cdot 10^{-9} \text{ m/s}$, $v = \lambda^3$, $n = 1.6 \cdot 10^{18} \text{ m}^{-2}$ and we suppose that $T = 20^\circ \text{ C} = 293^\circ \text{ K}$. The viscosity and surface tension are known. This leads to $A = 1.4 \cdot 10^{-1} \text{ m/s}$ and $B = 1.3$. The initial velocity ($0 \leq t \leq 0.1 \text{ s}$) matches experiment very well. Figure 7.16. The parameter n in equation 4.2 is estimated correctly, it denotes the number of adsorption sites per unit area. This is likely, because our experiments and those of Blake were both done on a glass surface. The contact line oscillates for too long afterwards. This causes capillary forces that counteract the oscillation at the centerline of the tube, which in turns causes large damping of that oscillation. The equilibrium height drops too low at the wall and thus remains too high in the middle. Another way to put this is to say that in the experiment the contact line has a larger damping and that it 'sticks' to a higher equilibrium position.

7.3 Contact angle hysteresis

According to all models, $\theta(t) = \theta_0$ implies that $h_t = 0$. In practice, $h_t = 0$ does not necessarily imply that $\theta(t) = \theta_0$. Experiments reveal that for a small region of $\theta(t)$ around θ_0 , the contact line sticks to one position. The domain in which the contact line sticks to the wall is $[\theta_R, \theta_A]$, where θ_R and θ_A are called the receding contact angle and the advancing contact angle respectively. The 'true' SCA lies within this domain. The presence and size of the domain is usually attributed to surface roughness of the boundary [29]-[32]. Figure 7.6 shows the sensitivity of the domain $[\theta_R, \theta_A]$. As noted previously, the contact line oscillates for too long and its equilibrium height is too low.

Without hysteresis, the contact line will drop, that is, has negative velocity if $\theta(t) \leq \theta_0$,

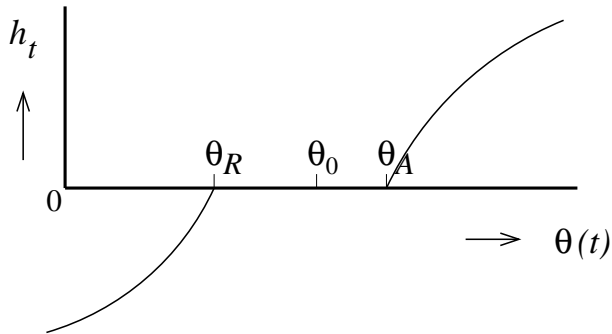


Figure 7.5: *Hysteresis: the contact line does not move whenever $\theta_R \leq \theta(t) \leq \theta_A$.*

according to equations 4.2 and 4.3. (Substitution of $A \rightarrow \infty$ in 4.2 yields 3.19). We analyse this experiment with hysteresis modelled. The contact line rises above the equilibrium height that matches with $\theta_0 = \theta_R$ (without hysteresis). This means, that after the contact line has reached its peak ($h_t = 0$), the contact line will drop. This is equivalent to $h_t \leq 0 \leftrightarrow \theta(t) \leq \theta_R$. This means the contact line drops until $\theta(t) = \theta_R$. In conclusion, for the equilibrium state it holds that $\theta_0 = \theta_R$.

A good model for hysteresis is not found, and even if it were, information about the boundary surface structure will be hard to find. We try an ad hoc domain. The hysteresis domain $[\theta_R, \theta_A] = [\cos \theta_0 + 0.075, \cos \theta_0 - 0.01] = [49.6^\circ, 55.7^\circ]$ gives very good results. Increasing the domain to $[\theta_R, \theta_A] = [\cos \theta_0 + 0.15, \cos \theta_0 - 0.02] = [43.6^\circ, 56.4^\circ]$ has too much effect. The contact line movement stops too early and the equilibrium height is far too high, as explained above. Fitting with experiment suggests that $[\theta_R, \theta_A] = [49.6^\circ, 55.7^\circ]$ and also that for $t \leq 0$ s no hysteresis should be modelled. If the measured angle lies within this domain, the contact line height is 'pinned' to its value of the previous time step.

In figure 7.6 the minimum at $t = 0.25$ s and the equilibrium height are bounded by θ_R . The first and the second peak are bounded by θ_A .

To avoid the long oscillation in time, contact angle hysteresis is applied as suggested above. Figure 7.7. The oscillation of the contact line stops right in time, the equilibrium height is correct and the centerline oscillation shows the right damping behaviour. Only the frequency is a bit too low, caused by the (slightly) too low CLV.

7.3.1 Static model with hysteresis

The inaccurate CLV cannot be corrected by the pinning conditions that are used with Blake's model. However, figure 7.8 shows that the influence of contact angle hysteresis with the static model has the same positive effect as for Blake. The oscillation of the contact line has decreased and the equilibrium height lies closer to the desired value. Technically, pinning is not relevant here. Pinning requires a measurement of the contact angle before it is set to θ_0 , thus using an extra variable to represent the contact line height. The static model uses no such variable, see chapter 9.

7.3.2 Billingham's model with hysteresis

The same hysteresis domain $[49.6^\circ, 55.7^\circ]$ is applied to Billingham's model. The parameter λ has no theoretical value and is fitted at 0.12 m/s. Compare figures 7.9 and 7.7. Blake

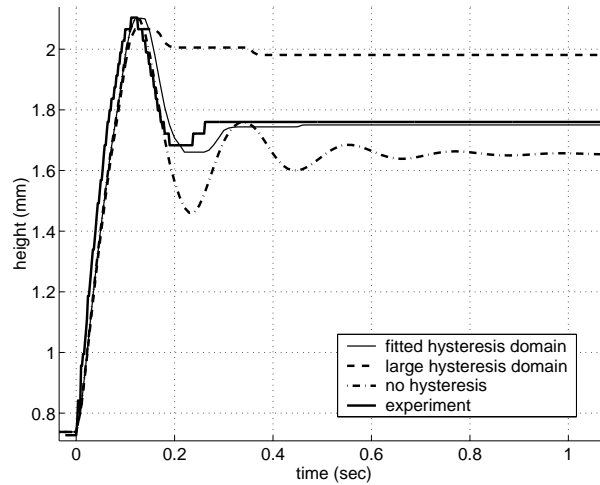


Figure 7.6: *M3 with Blake*. A large hysteresis domain matches the contact line with a greater equilibrium height. Without hysteresis the contact line oscillates for too long. The matching equilibrium height is too low.

and Billingham give the same results. This is in agreement with the velocity profile in figure 7.10, that shows the same behaviour for Blake and Billingham. The static model gives higher velocities, in agreement with the theoretical velocity profile. The theoretical velocity profile for the static model is obtained using the substitution $\lambda = \frac{\delta x}{2\delta t}$ in Billingham's model, see section 6.5.

7.4 Experiment with Detra

Detra has a small SCA ($\theta_0 = 5.5^\circ$). Near the wall, the grid is locally refined in order to calculate the sharp surface curvature in gravity, see section 6.3. A 40×60 and a 80×120 grid are used. For the 40×60 grid, the cells are locally refined in x -direction to an aspect ratio of $\frac{\delta y}{\delta x} \approx 3.1$. For the 80×120 grid, a small refinement of $\frac{\delta y}{\delta x} \approx 1.4$ satisfies. Without refinement, the uniform grid has an aspect ratio of $\frac{\delta y}{\delta x} \approx 1.3$. The SCA is adjusted to $\theta_0 = 7.2^\circ$ for the 40×60 grid, and to $\theta_0 = 7.3^\circ$ for the 80×120 grid, according to formula 6.13.

7.4.1 Static model

The results of the static model are shown in figure 7.11. As with the M3 experiment, the CLV is far too high, and as a result the centerline oscillation does not agree with experiment whatsoever.

7.4.2 Billingham's model

For Billingham's model, no theoretical estimation for its parameter can be made. Choosing parameter λ can be ambiguous. In figure 7.4.2 the behaviour of the model for different values of λ are shown. We choose $\lambda = 3 \cdot 10^{-3} \text{ m/s}$ with the largest overshoot for the contact line, but with the best results for the centerline, compared to experiment (figure 7.4.2). The high

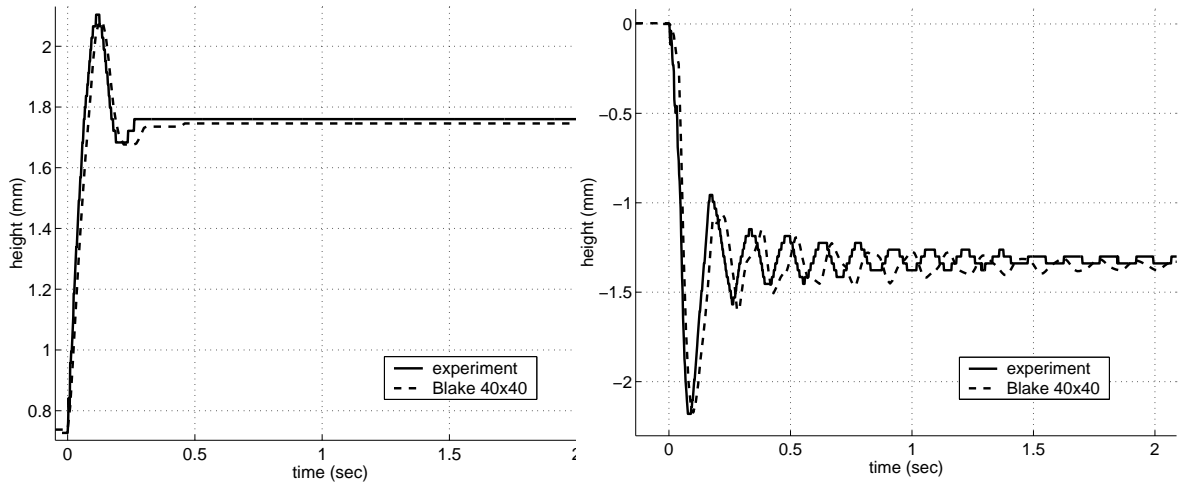


Figure 7.7: *M3 with Blake. Left: the contact line is pinned between $[49.6^\circ, 55.7^\circ]$. The oscillation of the contact line and the equilibrium height match experiment very well. Right: the centerline oscillation matches experiment well, except that the frequency is a bit too low.*

initial velocity gives an overshoot compared to the experimental contact line and Blake, due to the difference in the velocity profiles, chapter 4.1.

7.4.3 Blake's model

Detra is a mixture of 1234-tetrahydronaphtalene and decahydronaphtalene, and is not examined in Blake's paper. The test is done in a glass tube, as with M3, so n is considered to have the same (correct) value as with M3. The rest of the physical quantities in B are known, so after substitution of these quantities in B , we suppose that $B = 2.1$ is a correct value. The only parameters that are unknown are λ and κ_w^0 , see Appendix A. The first one varies with a factor 3 in Blake's work, the second one with a factor 100. The second one is not found in any literature for any of the two components of Detra, and has to be estimated. For the unknown parameters, we try the same values as for M3. This leads to the following estimate: $A = 1.6 \cdot 10^{-1} \text{ m/s}$ and $B = 2.1$ (figure 7.14). The estimated value of A leads to a highly inaccurate CLV.

Fitting with experimental data leads to the following values: $A = 4.3 \cdot 10^{-2} \text{ m/s}$ and $B = 2.1$. The results are very accurate and shown in figure 4.2. The oscillation frequency matches experiment, but the amplitude is a bit large, caused by the high CLV at $t = 0.5 \text{ s}$. Concluding that the CLV is predicted accurately by Blake, an indication of λ leads to a rough estimate of κ_w^0 and thus of ΔG_w^* , the molar activation free energy of wetting, see Appendix A. Perhaps this can give an indication for the free energy of similar liquids in case ΔG_w^* is unknown.

The velocity after $t = 0.5 \text{ s}$, with a correct initial velocity is a little bit too high, or, as Blake put it, the initial velocity is too small. A modification is made by Blake by adding parameters:

$$h_t = A \sinh\left(B\left[\cos \theta_0 - \cos \theta(t) + \frac{\beta \eta h_t}{\gamma}\right]\right) \quad (7.3)$$

With β some numerical coefficient and η the viscosity of the fluid. The new parameters represent the hydrodynamic effects that are neglected in the derivation of equation 4.1. These parameters correctly predict a higher maximum wetting velocity and a smaller maximum

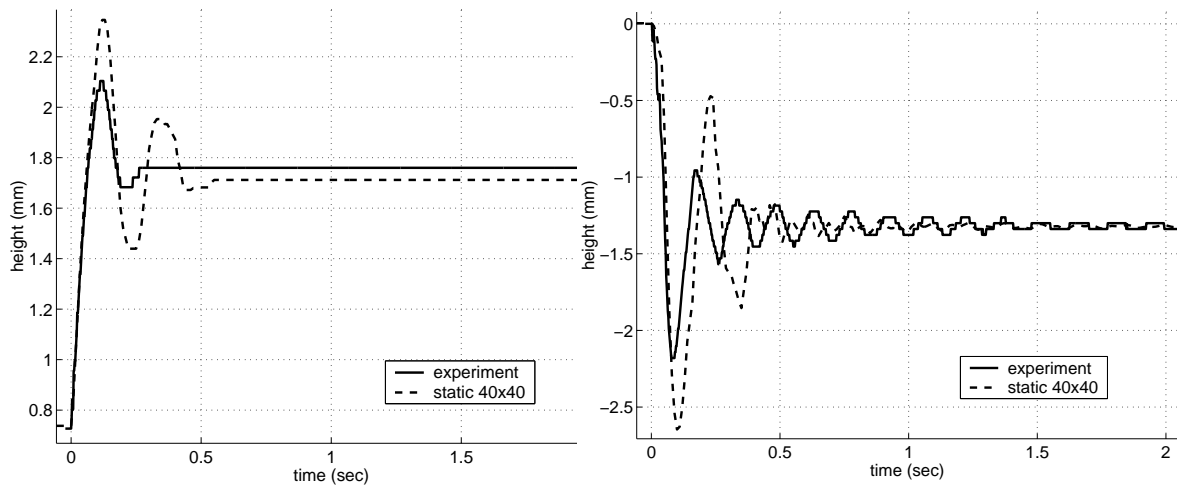


Figure 7.8: *M3 with the static model. Hysteresis is modelled. Left: the CLV is still too high, but the oscillation has decreased and the equilibrium height matches experiment better. Right: the oscillation at the centerline is still highly inaccurate (compare figure 7.3).*

dewetting velocity than equation 4.1, according to Blake [26]. Blake suggests that β is in the range of $[0.5, 1]$. The modification with $\beta = 1$ has no effect in our experiment, as figure 7.16 shows.

Figure 4.2 shows the liquid height at the centerline of the tube. The centerline oscillation of Blake shows slightly less agreement with experiment than Billingham. The centerline oscillation is driven by the motion of the contact line, so this result is surprising because the CLV is better predicted by Blake. In figure 7.17 the velocity profiles as a function of the capillary number are compared. Billingham's model predicts unbounded velocities at $\theta(t) = 180^\circ$, this is explained in section 4.4.

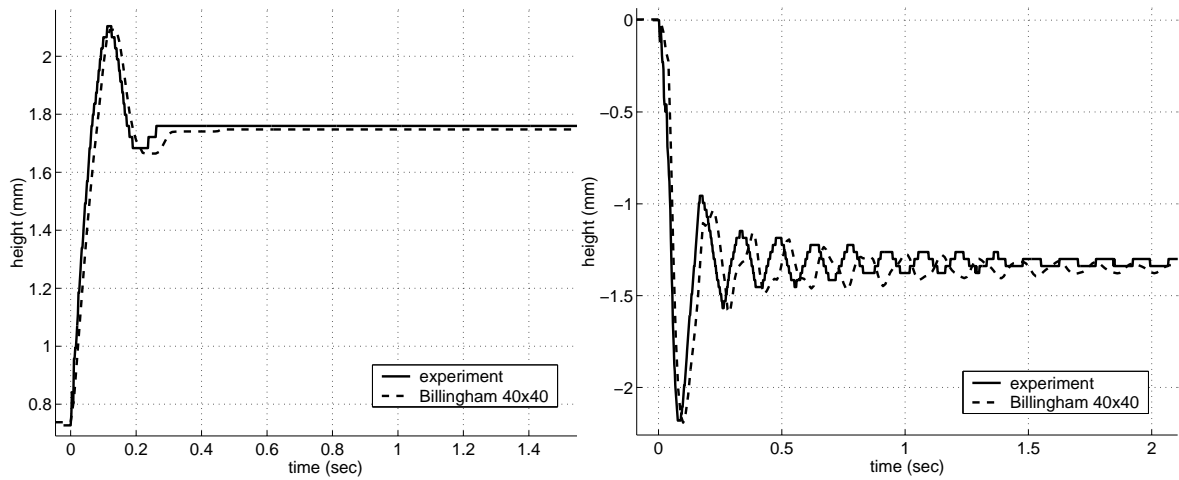


Figure 7.9: *Billingham for M3 with hysteresis. Left: the contact line. Right: the centerline oscillation. The outcomes with Billingham’s model match those with Blake, compare figure 7.7. This is consistent with the velocity profiles in figure 7.10.*

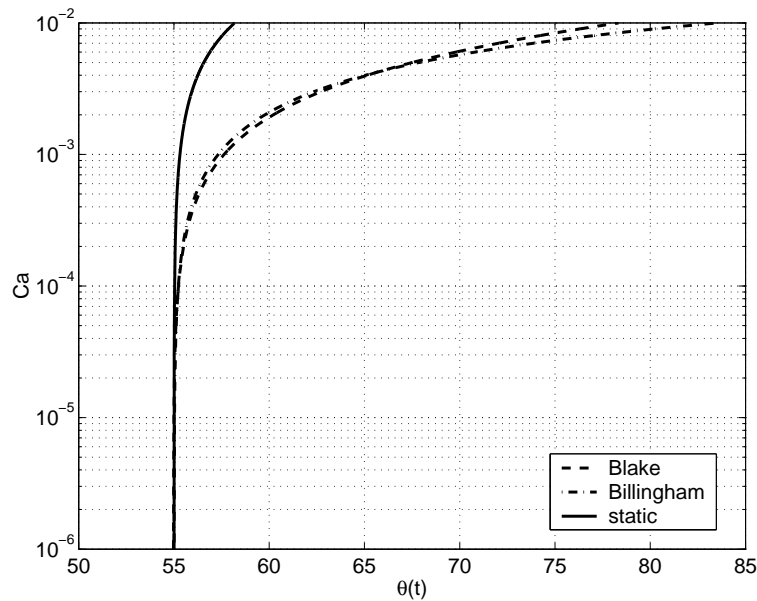


Figure 7.10: *M3. Velocity profiles of Blake, Billingham and the static model. No hysteresis effects are taken into account. Billingham and Blake behave very similar. The static model predicts far higher velocities. The profile of the static model is obtained by the substitution $\lambda = \frac{\delta x}{2\delta t}$ in Billingham’s model, see section 6.5.*

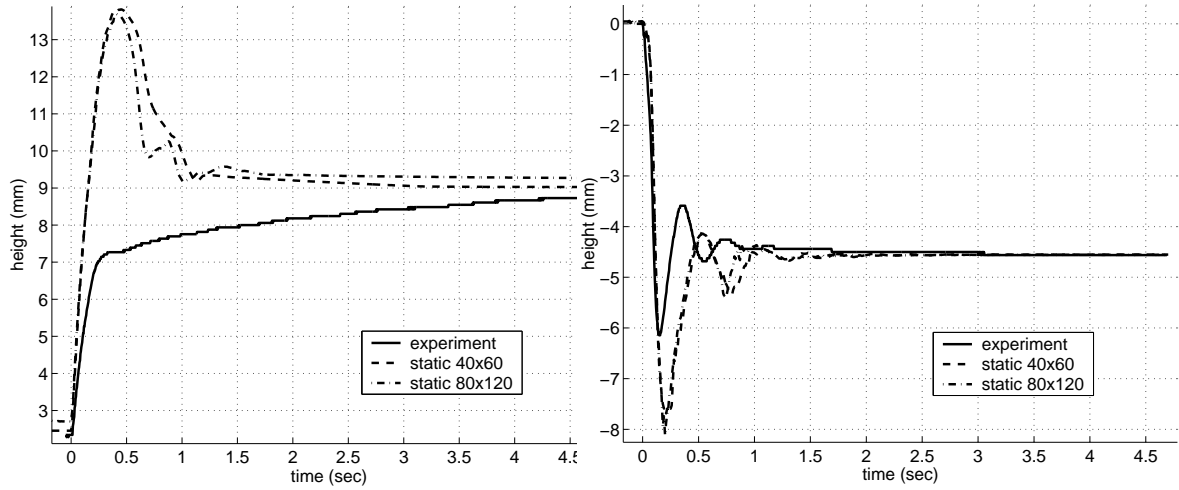


Figure 7.11: *Static model for Detra. The CLV is far too high (left), and as a result the centerline oscillation does not agree with experiment whatsoever (right).*

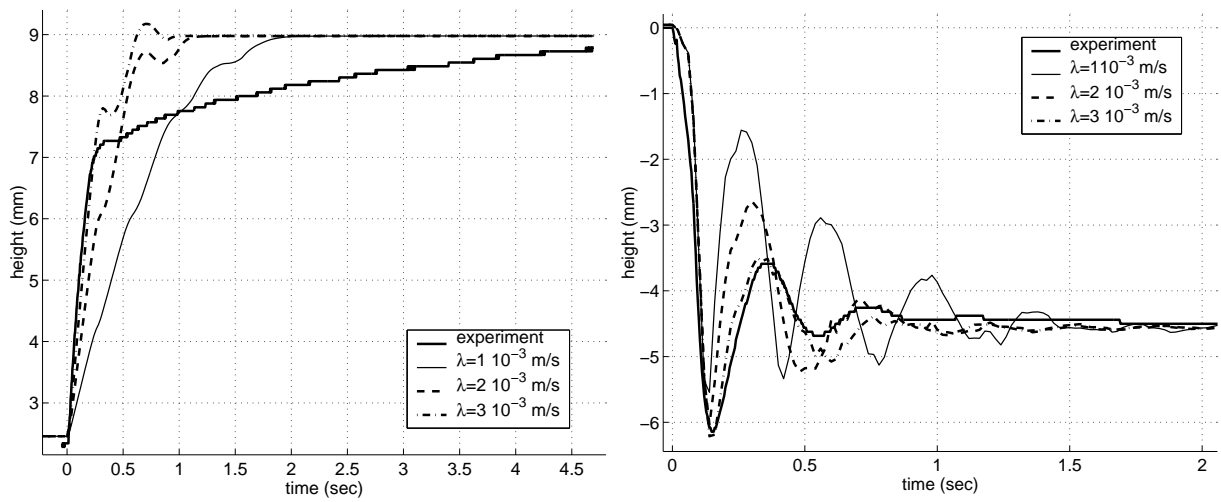


Figure 7.12: *For different values of λ , Billingham's model is tested. $\lambda = 3 \cdot 10^{-3} \text{ m/s}$ has the most accurate centerline oscillation.*

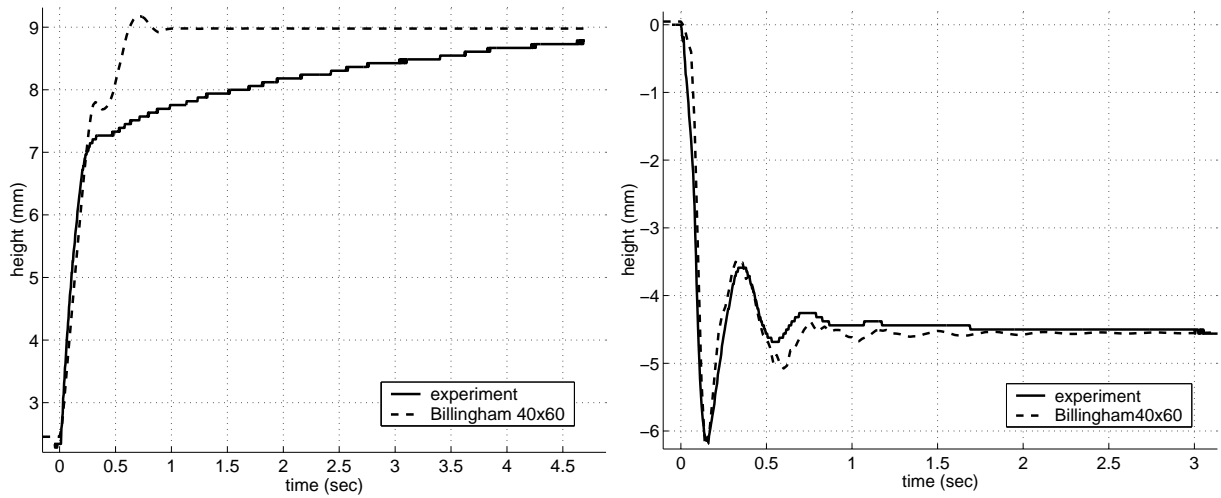


Figure 7.13: *Detra* with *Billingham* ($\lambda = 3 \cdot 10^{-3}$ m/s). The centerline oscillation is in good agreement with experiment (right), although the CLV shows some inaccuracy (left).

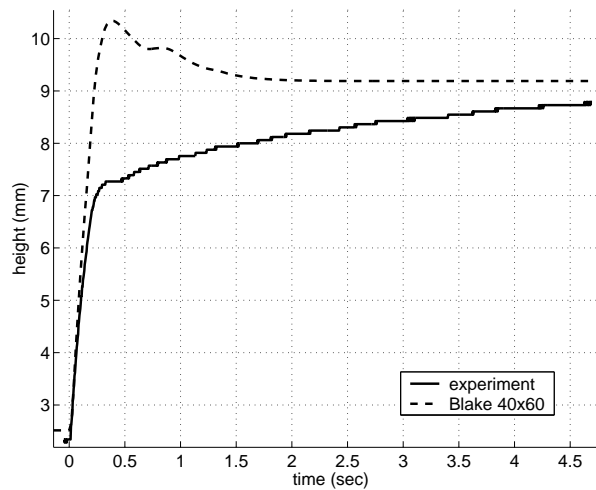


Figure 7.14: *Detra* with *Blake*. The estimated values for *A* and *B* lead to a highly inaccurate CLV.

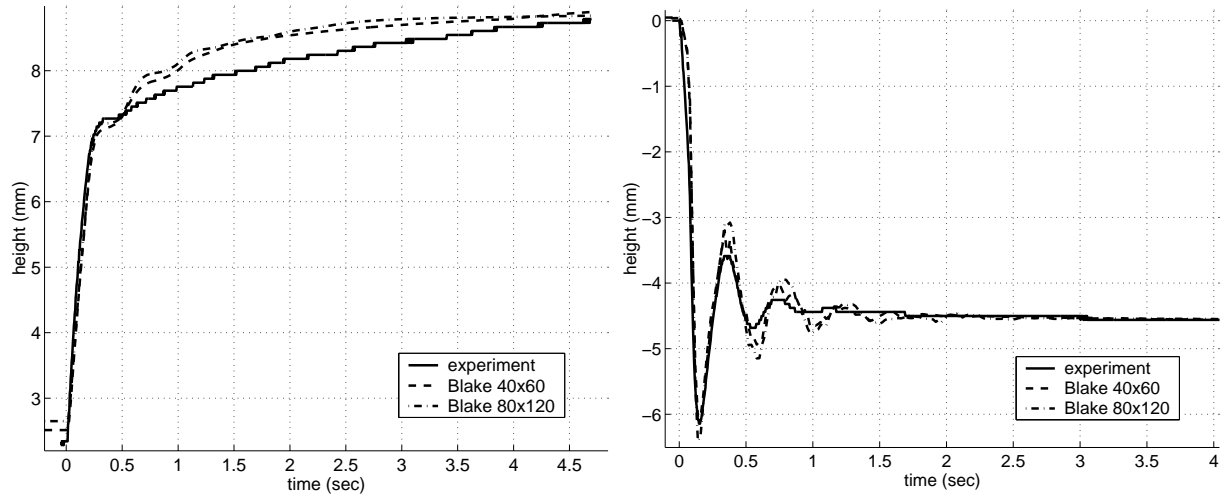


Figure 7.15: *Detra with Blake. Left: the contact line height. The difference with experiment is small for both grids. Right: height in the middle of the tube. The frequency matches experiment, but the amplitude is too high, caused by the high CLV at $t = 0.5$ s.*

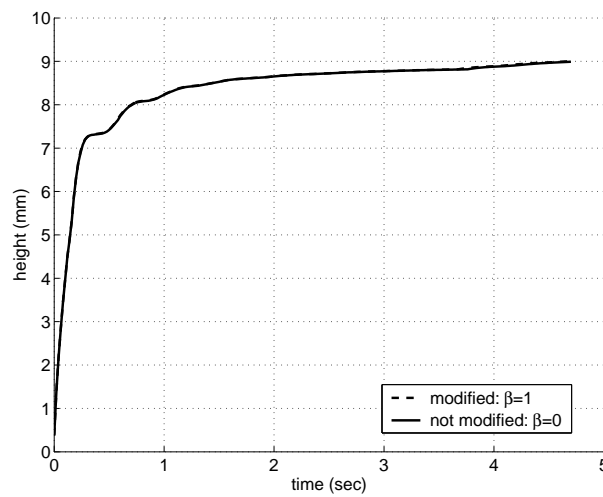


Figure 7.16: *The modification of Blake's model with $\beta = 1.0$ has no effect.*

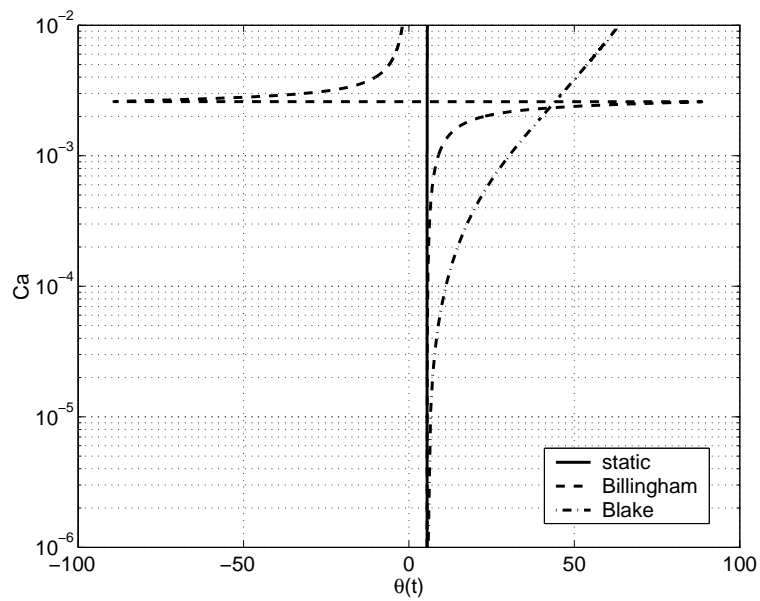


Figure 7.17: *Detra*. Velocity profile of Blake's, Billingham's and the static model as a function of the DCA. The velocity is represented by the capillary number, $Ca = \frac{\eta b_t}{\gamma}$. The static model predicts an almost infinite velocity at all times. Up to $\theta(t) = 30^\circ$, Billingham's velocity is higher than Blake's. For higher contact angles it is the other way around. At 180° , Billingham tends to infinity, as explained in section 4.4. A negative angle $-\theta$ degrees means $180 - \theta$ degrees.

Chapter 8

Testing with experiment: empirical models

In this chapter the empirical models from Seeberg, Jiang and Bracke (see chapter 5) are tested numerically by means of two experiments with Detra and M3. The experiments are the same as in chapter 7. The simulations are done under the same conditions as in chapter 5.

8.1 Experiment with M3

Blake's model is compared to the models from chapter 5. Because these models only describe positive contact line velocity, negative CLV is modelled by Blake's model. The adjustment for the model by Seeberg gives lower CLV's for low capillary numbers, according to Seeberg [18]. Figure 8.1 shows indeed lower CLV's for the adjusted model. Only the first peak of the contact line is shown, compare figure 7.16. In this case, the adjustment has negative effect. Therefore no adjustment is applied to Seeberg's model for M3. Hysteresis is modelled as in chapter 5, but does not have significant effect for $0 \leq t \leq 0.12$ s.

Figure 8.3 shows the results with hysteresis modelled and without the adjustments of Seeberg at low capillary numbers. Blake has the greatest velocity and gives the best prediction of the wetting velocity, followed by Jiang, Seeberg, and Bracke, in that order. Jiang's is the oldest of the empirical models, but is in this particular case most accurate. This emphasizes the large scattering of data on which the empirical models are based. The numerical outcomes are justified by the (theoretical) velocity profiles in figure 8.4. The theoretical curves show that for near-equilibrium contact angles Blake has the greatest CLV, followed by Jiang, Seeberg, and Bracke. The centerline oscillation is not shown. All models follow the theoretical velocity profile in a qualitative way. This means that different behaviour for individual models at the centerline does not have significant influence on the motion of the contact line. In other words: erroneous behaviour of the contact line is not caused by erroneous behaviour of the centerline height.

8.2 Experiment with Detra

Figure 8.5 shows that the adjustment for Seeberg's model has negative effect, so no adjustment is applied this time. Figure 8.6 shows the results of the experiment with Detra. Blake's model predicts the most accurate wetting velocity. Seeberg and Bracke predict a far too

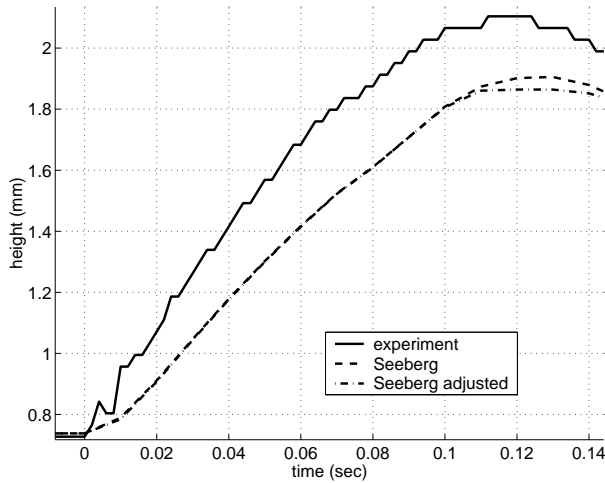


Figure 8.1: *M3 (contact line). The model of Seeberg is adjusted for low capillary numbers, with negative effect.*

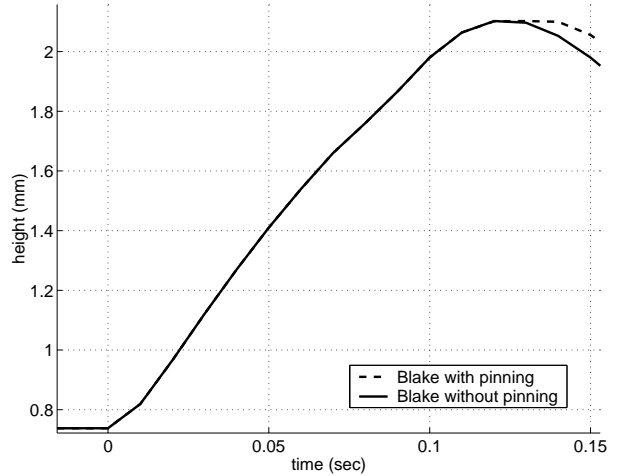


Figure 8.2: *Blake with M3. Hysteresis has no significant effect for $0 \leq t \leq 0.12$ s.*

small velocity near equilibrium. Jiang's is again most accurate of the empirical models. The computational results agree with the theoretical velocity profiles in figure 8.6. For large deviations of the SCA, Blake's model implies a much smaller CLV. Near equilibrium, Blake implies the greatest velocity, followed by Jiang, Seeberg and Bracke, in that order. At the time gravity is released, $\theta(t) = \theta_0$, and it is very well acceptable to assume that $\theta(t)$ does not deviate much from its static value during the experiment.

8.3 Error percentages

The computational results are plotted to give an intuitive idea of the accuracy of the models. The accuracy in liquid height as a function of the time can be denoted by a number that represents the error of the liquid height with respect to the experimental height as a percentage. This number is called P and is defined as the percentual difference between the computed and experimental liquid height over the whole time interval, so the difference in contact line height is

$$P \equiv \frac{1}{T} \int_0^T v dt \quad (8.1)$$

Where we define

$$v = \left| \frac{h_w^e - h_w}{h_w^e} \right| \quad (8.2)$$

with h_w^e and h_w the experimental and computed contact line height respectively. P is discretized as

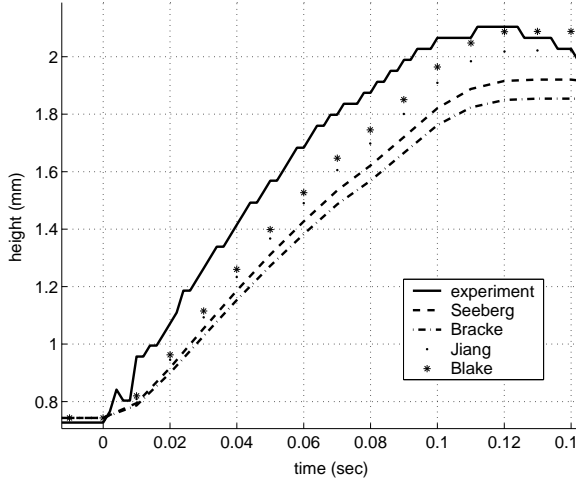


Figure 8.3: *M3. The contact line behaviour of the models from Seeberg, Jiang and Bracke is compared to that of Blake and the experimental values. Blake’s results are most accurate. Hysteresis is modelled.*

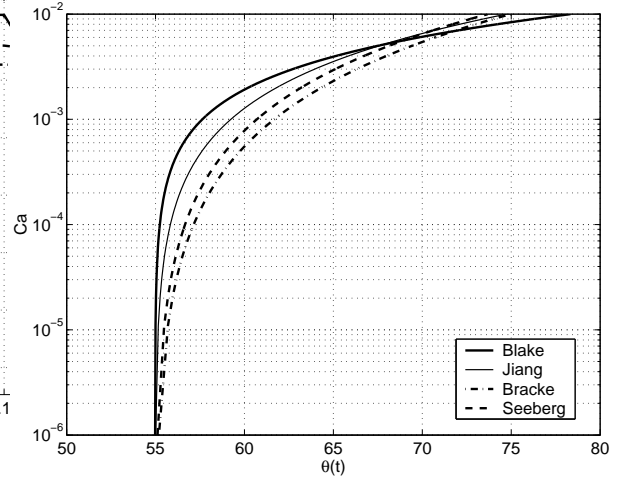


Figure 8.4: *Velocity profile for M3 for Seeberg, Bracke, Jiang and Blake. Blake predicts the highest velocity, followed by Jiang, Seeberg and Bracke respectively.*

$$P \equiv \frac{1}{T} \sum_{i=0}^n v_i \delta t = \frac{\delta t}{T} \sum_{i=0}^n v_i \quad (8.3)$$

$$= \frac{1}{n+1} \sum_{i=0}^n v_i \quad (8.4)$$

Where δt is constant. This is the trapezoidal rule, which gives each time step an error of

$$E = \frac{\delta t^3}{12} \frac{\partial^2 h_w}{\partial t^2} \quad (8.5)$$

with $v_i = v(t = i\delta t)$ and $T = n\delta t$. The experimental data points have a distance of 0.004 s and 0.002 s for Detra and M3 respectively. This means that n is large enough for equation 8.4 to approach equation 8.1 sufficiently, to neglect the interpolation error that is made by using the first one. The percentages are given in figure 8.7. For the experiment with M3, the results for $T = 0.5$ s are as expected: Blake is most accurate, followed closely by Billingham, Jiang, Bracke and Seeberg in that order. After $t = 0.5$ s, the contact line does not move so including this time interval does not contribute to the error analysis. The static model shows an error almost four times the size of the error with Blake’s model. The empirical models only prescribe positive CLV, so their accuracy is best shown with $T = 0.12$ s, so only the first peak. Remarkably, the static model is most accurate for this small interval. Blake’s and Billingham’s model are by far most accurate, and only Jiang’s model shows a reasonable error. Bracke and Seeberg both give a very large error. For Detra, Blake’s model seems to be most accurate by far, according to the plots, but not according to the percentual error.

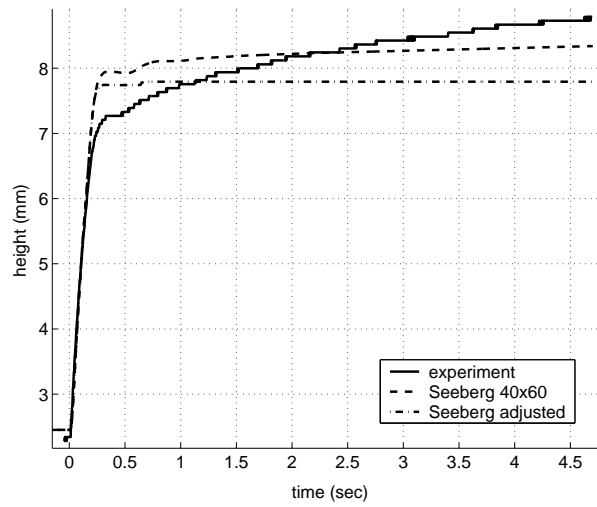


Figure 8.5: *Detra*. The model of Seeberg is adjusted for low capillary numbers. The adjustment has negative effect.

Seeberg's model has an equally large error, which can also be seen from the plots. However, for larger T , figure 8.6 implies that Seeberg loses accuracy very rapidly because the contact line is almost static after $t = 1$ s, in contrast to Blake's model. When Seeberg's model is adjusted for low capillary numbers, the error percentage increases from $P = 3.4$ % to $P = 7.7$ % (see also figure 8.5).

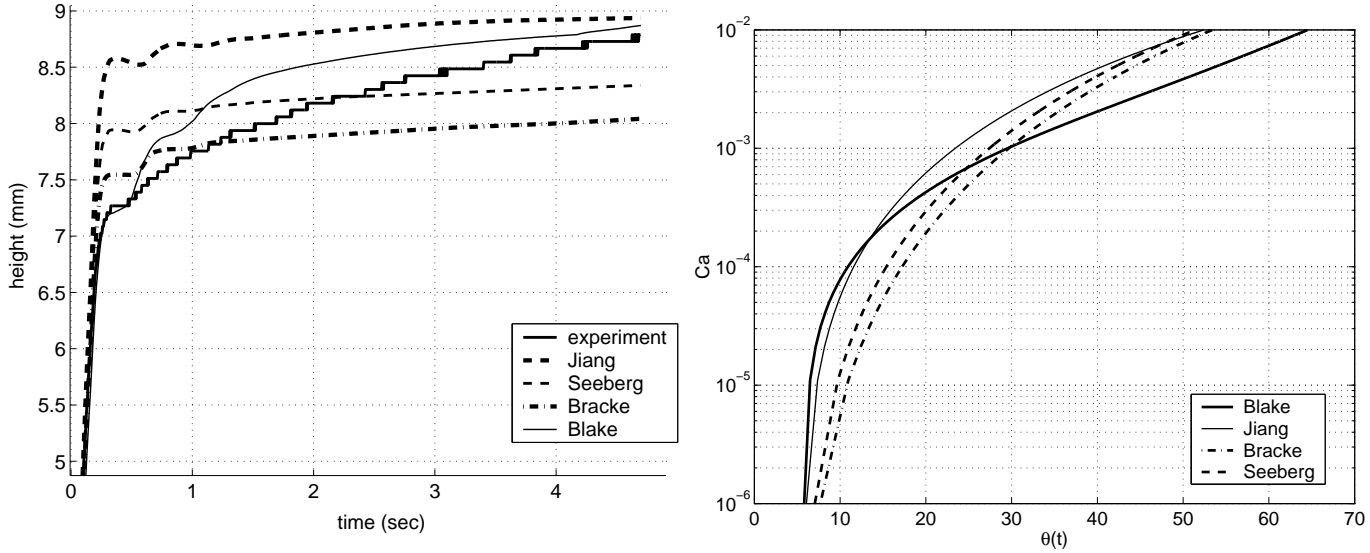


Figure 8.6: *Left: Detra. From top to bottom at $t = 4.5$ s: Jiang, Blake, experiment, Seeberg and Bracke. Blake is most accurate of all. The near-equilibrium velocity predicted by Seeberg and Bracke is far too low. The curves are in agreement with the velocity profile at the right. Right: Velocity profile for Detra for Seeberg, Bracke, Jiang and Blake. The CLV is represented by the capillary number. With a large DCA, Blake predicts a much smaller velocity than the other models. Near equilibrium, Seeberg and Bracke predict very low velocities.*

	Static	Bracke	Seeberg	Jiang	Billingham	Blake
M3 ($T = 0.5$ s)	12.3	6.0	7.2	4.1	3.4	3.3
M3 ($T = 0.12$ s)	5.2	16.4	15.6	10.4	7.7	7.2
Detra ($T = 4.7$ s)	22.8	4.9	3.4	9.0	9.9	3.4

Figure 8.7: *Error percentages of the contact line height of the DCA models. The bold-faced numbers denote the smallest percentages.*

Chapter 9

Implementation methods

Implementing the DCA models into the numerical code is not a straightforward matter. Let us first consider the static model. For all surface cells at the wall, the SCA is applied in the following manner. First, the orientation of the fluid is determined for the surface cell, i.e. the fluid is above or below the surface. Thereafter, the angle between the surface and the wall is set to θ_0 . This method is implemented straightforwardly and the model works in every situation. A DCA model has a relation of the form

$$h_t = f(\theta(t)) \quad (9.1)$$

Which can be discretised in two ways

- θ^n (at time $t = n\delta t$) is stored by means of h_w^n , the contact line height. Consider time step $n + 1$. The surface pressure is calculated, with the dynamic contact angle as a boundary condition, see section 3.7. θ^n is calculated by means of h_w^n and h_i^n . Equation 9.1 implies the contact line velocity (CLV), h_t , and so h_w^{n+1} . Now, the N-S equations are solved and a new h_i^{n+1} can be calculated.
- No variable is used for the contact line. Instead, θ^n is measured by means of h_i^n and h_{i-1}^n . Equation 9.1 implies h_t , and so h_{i+1}^{n+1} . Now, the N-S equations are solved and the new h_i^{n+1} and h_{i-1}^{n+1} can be calculated.

The first method is now used, for it is numerically accurate and physically the CLV is considered a local phenomenon. A great disadvantage is that the dummy h_w is stored. Multiple contact lines, have to be matched with multiple h_w 's. This can be quite cumbersome. Think of a sloshing liquid, where contact lines appear and disappear or move towards each other, or come together and disappear.

The second method works in all situations. Physically it is incorrect, for the DCA is not defined exactly at the wall. Velocities within the fluid domain have too much influence on the contact line dynamics. Results are not shown, but are far from satisfactory.

A third possibility is to invert relation 9.1, to obtain the form $\theta(t) = f^{-1}(h_t)$ with input h_t instead of $\theta(t)$. Let us investigate Blake's model. The inverted form of formula 4.2 becomes

$$\cos \theta(t) = \cos \theta_0 - \frac{1}{B} \ln\left(\frac{h_t}{A} + \sqrt{\frac{h_t^2}{A^2} + 1}\right) \quad (9.2)$$

h_t cannot be defined exactly, but is approximated by $v(i, j)$, the vertical velocity in cell (i, j) . This method has three drawbacks:

- the approximation error $h_t \approx v(i)$.
- for large h_t , $\theta(t)$ is very sensitive for small input errors, compare figure 8.4.
- the input h_t is bounded. For $\theta_0 \rightarrow 0$ this means for equation 9.2, that the input cannot have negative values.

Figure 9.1 shows that the accuracy of the inverted model of Blake reduces with the SCA. A step reduction of the gravity with Detra is simulated. Whenever 9.2 is unsolvable, Billingham's model is applied. This is the case when $\frac{h_t}{A} + \sqrt{\frac{h_t^2}{A^2} + 1} \leq 0$ or when $\cos \theta(t) \geq 1$. Figure 9.2 shows that for small SCA's, Blake's model only allows small maximum dewetting velocities. Billingham's model allows any velocity because $\cot \theta$ is unbounded. Large negative velocities simply imply a small $\theta(t)$. The simulation with $\cos \theta_0 = 5.5^\circ$ has the largest contact line velocities and the most sensitive $\cos \theta(t)$ as a function of negative CLV, see figure 9.2. This explains the inaccuracy in figure 9.1. Note that the peaks in figure 9.1 are not a result of the transition between Blake and Billingham, but of the sensitivity of $\theta(t)$ as a function of $v(i, j)$.

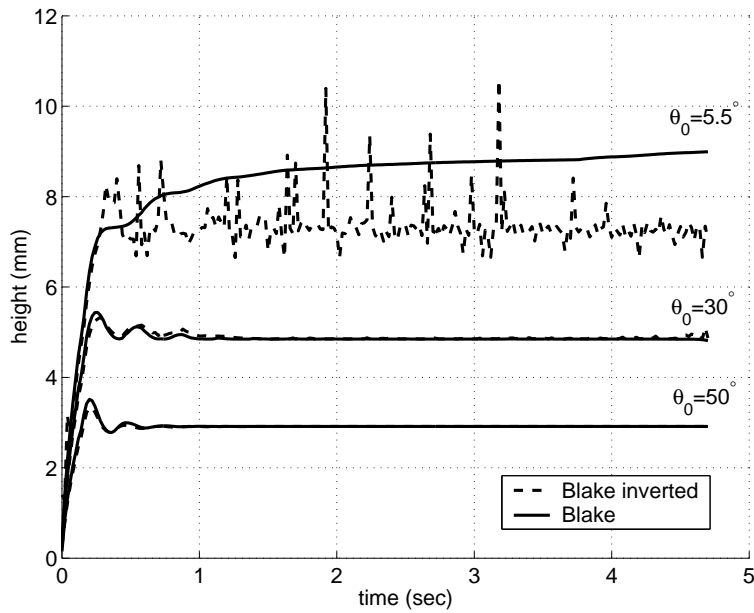


Figure 9.1: *Detra*. For large SCA's the inverted model is accurate. For small SCA's, the inverted model becomes inaccurate.

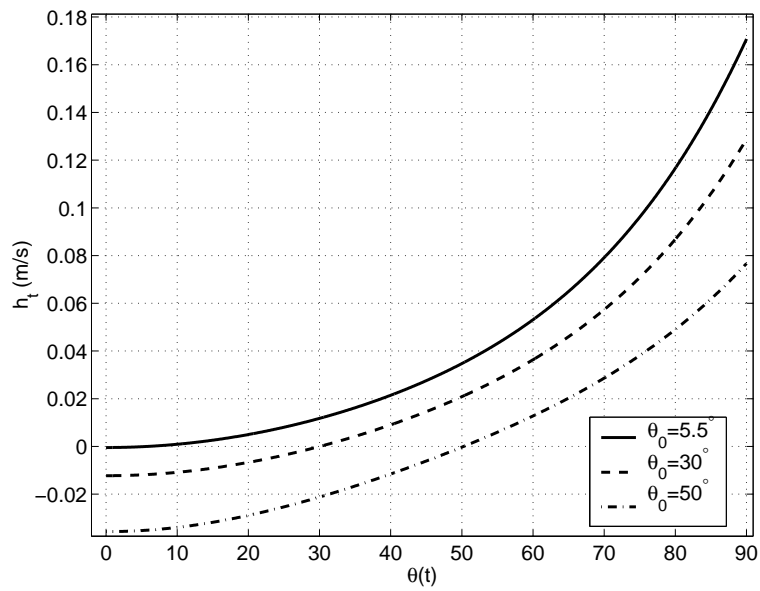


Figure 9.2: *Blake*. For small SCA's, only high velocities can be inverted, and the inverted model is sensitive for small errors at low velocities.

Chapter 10

Discussion and recommendations

The simulation results agree with the theoretical velocity profiles. This means that the code with the DCA as a local boundary condition of the surface is numerically valid. The experiments with Detra and M3 only cover situations with small capillary numbers. These are the most important situations for testing the validity of DCA models, because then the surface tension forces dominate the kinetics of the liquid.

The static model is most straightforward in implementation, because no contact line is modelled and no information from previous points in time have to be stored, see chapter 9. The outcomes of the tests imply however, that with small Capillary and Bond numbers, the static model gives highly inaccurate results. The very high CLV of the static model, compared to the dynamic models is explained physically. The use of a variable for the contact line height makes implementation for multiple contact lines laborious. This can be avoided by inverting Blake's model. For small SCA's, an inverted model appears to be insufficient because of sensitivities of the DCA for small CLV's. The original model works for all SCA's, and guarantees accuracy and stability.

For the empirical models, scattering of reference data plays an important role. This is illustrated by the fact that in the experiment with M3, Jiang gives the most accurate results, while it is the oldest model, based on the least amount of data. A certain accuracy is in theory guaranteed by empirical models, and the results confirm this. No parameters have to be fitted, which is an advantage when experimental data are unavailable and it saves a lot of preparation time. A drawback is that no negative CLV is modelled. Blake's model is most accurate of all. The price to pay for this, is that two parameters have to be determined. The model has a solid physical background. The theoretical substance-related coefficients depend on more than ν , σ and θ_0 as empirical models suggest. The large deviation of these coefficients for individual fluids explains the large scattering in the experimental data in comparison to empirical curves. These coefficients are often unknown or hard to find for individual fluids, in that case they have to be fitted with experiment.

Contact angle hysteresis has a large influence on the outcomes of the experiment with M3. Hysteresis is usually attributed to roughness of the solid surface. By choosing a suitable hysteresis domain $[\theta_R, \theta_A]$, we can simulate the experiment with M3 very well, but the choice is always ad hoc. No suitable models are yet available, and even if they were, information about the surface structure/roughness of the boundary, which is hard to retrieve, would be required.

10.1 Practical model

As is discussed above, the different models have different advantages and drawbacks. These are summarized below.

model	advantages	drawbacks
Blake	-highly accurate -generally valid*	-two free parameters
Billingham	-accurate -almost generally valid**	-one free parameter
Empirical	-reasonably accurate -no free parameters	-only positive CLV

* Generally valid with respect to velocities. Multiple contact lines are difficult to implement, see chapter 9.

** Problems arise when $\theta_0 \rightarrow 0$ or when $\theta(t) \rightarrow 180^\circ$, see section 4.1.

Our wish is to find a model that is practically applicable without unnecessary fitting of free parameters. This saves time and no experimental data are required. The idea is to obtain a least squares fit of Blake's model to an empirical model. The parameters of Blake then only depend on ν , σ and θ_0 like with the empirical model. The negative CLV can be modelled by Blake and the positive by an empirical model. The kinetics of the contact line are completely determined by the code with an option of fitting Blake's parameters if desired. For an empirical model, Seeberg's is chosen because it is the most recent one (1992) and Seeberg compares her model to those of Jiang and Bracke. A least squares fit of Blake's model is applied to Seeberg over a regime of the capillary number:

$$\text{Seeberg: } S = \cos \theta_0 - \cos \theta(t) = [\cos \theta_0 + 1]2.24Ca^{0.54} \quad (10.1)$$

$$\text{Blake: } B = \cos \theta_0 - \cos \theta(t) = \frac{1}{B} \sinh^{-1}\left(\frac{\sigma Ca}{A\nu}\right) \quad (10.2)$$

$$I(A, B) = \int_{Ca_{min}}^{Ca_{max}} [S - B]^2 dCa \quad (10.3)$$

$$(10.4)$$

Parameters A and B are found by solving the minimum of this integral:

$$\frac{\partial^2 I}{\partial A \partial B} = 0 \quad (10.5)$$

Equation 10.5 is solved with Mathematica[©]. Seeberg based her correlation on experimental results in the regime $0 \leq Ca \leq 3 \cdot 10^{-2}$. Above this range, the contact line loses its dominance over the kinetics of the fluid. For very low Ca ($\leq 10^{-3}$), Seeberg adjusted her model a slight bit. However, since this adjustment had no significant influence on the outcomes of the simulated experiments in chapter 8, and for convenience reasons, Seeberg's model will be used without adjustment in this chapter. In theory, $[Ca_{min}, Ca_{max}] = [10^{-3}, 3 \cdot 10^{-2}]$. The real solutions are extremely sensitive with respect to the upper boundary Ca_{max} , because for small Ca , $\frac{1}{B} \sinh^{-1}\left(\frac{\sigma Ca}{A\nu}\right) \approx \frac{\sigma Ca}{BA\nu}$. The product AB is less sensitive for variations of Ca_{max} , as

Ca_{max}	A	B	AB	λ
0.01	$\frac{\sigma}{117.2\nu}$	$\frac{4.6}{[\cos \theta_0 + 1]}$	$\frac{0.039\sigma}{\nu[\cos \theta_0 + 1]}$	$\frac{0.046\sigma}{\nu[\cos \theta_0 + 1]}$
0.02	$\frac{\sigma}{58.6\nu}$	$\frac{3.2}{[\cos \theta_0 + 1]}$	$\frac{0.055\sigma}{\nu[\cos \theta_0 + 1]}$	$\frac{0.063\sigma}{\nu[\cos \theta_0 + 1]}$
0.03	$\frac{\sigma}{39.1\nu}$	$\frac{2.5}{[\cos \theta_0 + 1]}$	$\frac{0.064\sigma}{\nu[\cos \theta_0 + 1]}$	$\frac{0.075\sigma}{\nu[\cos \theta_0 + 1]}$

Figure 10.1: *Blake's model and Blake's first order model are fitted to Seeberg's model for positive CLV. λ , A and B are functions of Ca_{max} . λ behaves similar to AB.*

table 10.1 shows. For large Ca , a small variation of A or B has large influence on $A \sinh(B)$, even if their product remains constant. A Taylor series gives

$$A \sinh(B[\cos \theta_0 - \cos \theta(t)]) = AB[\cos \theta_0 - \cos \theta(t)] + AB^3[\cos \theta_0 - \cos \theta(t)]^3 + AB^5 \dots \quad (10.6)$$

which shows the dominance of the first term when $B[\cos \theta_0 - \cos \theta(t)]$ is small. We take only the first term and match it with Seeberg:

$$\text{Seeberg: } S = \cos \theta_0 - \cos \theta(t) = [\cos \theta_0 + 1]2.24Ca^{0.54} \quad (10.7)$$

$$\text{Blake first order: } B = \cos \theta_0 - \cos \theta(t) = \frac{\sigma Ca}{\lambda \nu} \quad (10.8)$$

$$I(\lambda) = \int_{Ca_{min}}^{Ca_{max}} [S - B]^2 dCa \quad (10.9)$$

Note the similarity with Billingham's model. Table 10.1 shows that λ behaves the same as the product AB . This means that for fitting purposes, only the first term is important. So far, the first component of the Taylor series of Blake's model is fitted to Seeberg's model by a least squares fit over a domain of the capillary number. This domain influences the magnitude of the fitted parameter λ very much. Approximation of equation 10.9 gives

$$I(\lambda) = \int_0^{Ca_{max}} [\alpha Ca^{0.54} - \frac{1}{\lambda} Ca]^2 dCa = \int_0^{Ca_{max}} Ca^2 [\frac{\alpha}{Ca^{0.46}} - \frac{1}{\lambda}]^2 dCa \quad (10.10)$$

With α a given quantity. This means that for a minimum value of I , λ increases with Ca_{max} . Figure 10.2 shows the effect of the differences in λ for the Detra experiment.

The CLV is too high. However, negative CLV is now modelled by Blake. Without fitting any parameters, Seeberg models the positive CLV, and Blake models the negative CLV. A second option is to 'mirror' Seeberg's model for negative CLV:

$$CLV \geq 0 : \frac{\cos \theta_0 - \cos \theta(t)}{\cos \theta_0 + 1} = 2.24Ca^{0.54} \quad (10.11)$$

$$CLV \leq 0 : \frac{-\cos \theta_0 + \cos \theta(t)}{\cos \theta_0 + 1} = 2.24[-Ca]^{0.54} \quad (10.12)$$

$$(10.13)$$

The results of Seeberg's model for Detra and M3 are known. For M3 without hysteresis, we assume that Blake's model with fitted A and B is accurate, because it is when hysteresis

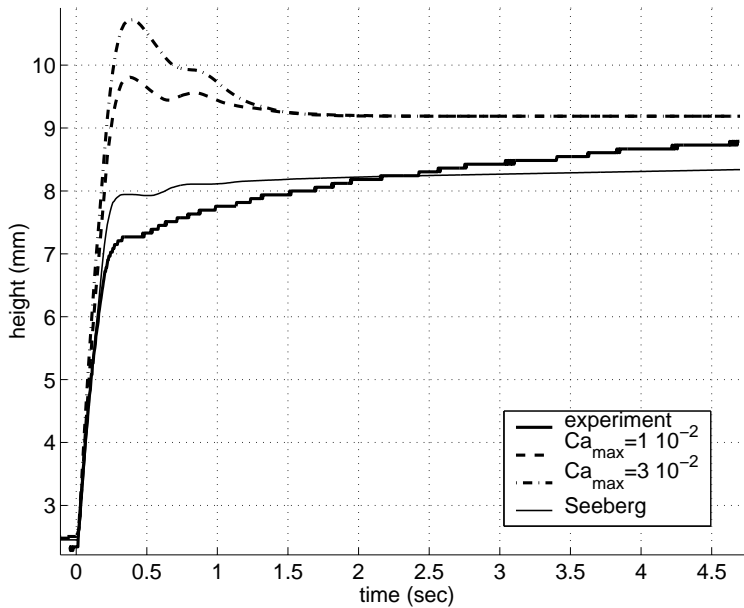


Figure 10.2: *Detra*. Blake first order, fitted to Seeberg. The fitted λ 's produce a large CLV. Seeberg is more accurate.

effects are taken into account. Hysteresis is not modelled to emphasize the negative CLV. The two practical models that are described above, are tested for negative CLV. The positive CLV is modelled by model of Blake with fitted A and B . The negative CLV is modelled by Blake's fitted first order model and by Seeberg's mirrored model. The two models are compared to the results of Blake's model for all CLV's with fitted A and B . Figure 10.3 shows the difference between the different values of λ , the values A and B from Blake's model and Seeberg's mirrored model.

Seeberg's mirrored model behaves differently than Blake's first order model. The latter matches Blake's model very well for all λ . In this test it seems worthwhile to use Blake's first order model instead of Seeberg's mirrored model for negative CLV. There are now three reasons to use Blake's first order model for negative CLV, instead of Seeberg's mirrored model. Firstly, Blake's velocity profile has theoretical background. Secondly, Seeberg's model is fit only to positive CLV. Thirdly, Seeberg's mirrored model does not seem to agree with experiment, and Blake's first order model does. The applicability of the model is disturbed by the contact line hysteresis, a property that is usually contributed to the roughness of the solid surface. As seen in the M3 experiment, hysteresis has a large influence on the kinetics of the DCA. A generally valid hysteresis model has not been found yet. Even if this was the case, the solid surface structure is hard to retrieve. We know that hysteresis occurs and that it can have a large influence. Whether it occurs only with large SCA's, with M3, and not with Detra, remains unknown. Detra shows no hysteresis, for the contact line is always moving. Figure 10.4 shows the small effect of hysteresis, with the domain $[\theta_R, \theta_A] = [\theta_0 - 5.4^\circ, \theta_0 + 0.7^\circ]$, the same as for M3. The ad hoc domain has good influence with M3 and no significant influence with Detra. Only at the end of the simulation the contact line seems to stop moving under the influence of hysteresis.

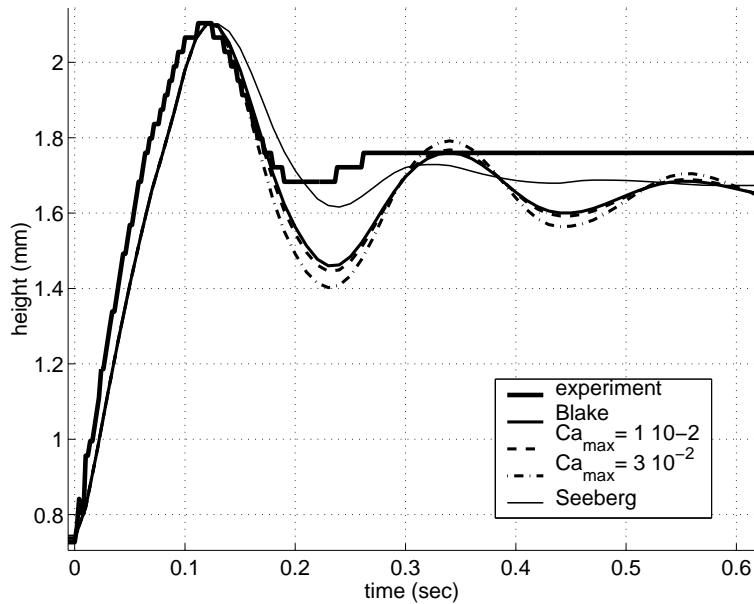


Figure 10.3: *M3. Positive CLV is modelled by Blake’s model. Negative CVL is modelled by Blake’s first order model, and Seeberg’s mirrored model. No hysteresis is modelled in order to emphasize the negative CLV. Blake’s first order model matches Blake’s model very well. Seeberg’s model behaves completely different.*

10.2 Conclusions and recommendations

With the use of Blake’s model, of which the accuracy has been proven in Blake’s work, together with experimental results and an ad hoc hysteresis domain, it is shown that our current code generates results that agree with physical reality very accurately in two test cases. The different results that have been accomplished with different models, are in excellent agreement with theoretical predictions. The implementation of the contact angle models as a local boundary condition is in conclusion a very successful method. We have an indication that with the current code it is very well possible to investigate accuracy, behaviour and influence of different contact angle models.

According to the extensive validation of Blake’s model in Blake’s work, and its physical background, we are confident that with Blake’s model implemented in our VOF code, we are in general able to obtain accurate results in case of a low Bond- and capillary numbers. This is also the case in which the modelling (error) of the DCA has the largest influence on the liquid kinetics. Therefore we have good hope that the code with Blake’s DCA model will produce accurate results in many different situations.

When experimental material is available, unknown parameters can be fitted for an optimal result, as was the case with the experiment with Detra. Also the hysteresis domain can be fitted according to experimental data.

When not all properties are available in Blake’s model, I would recommend a combined model, that describes positive CLV according to Seeberg’s model and negative CLV according to Blake’s first order model that is fit to Seeberg’s model. Both positive and negative CLV’s are correctly prescribed on a large enough range of the capillary number. An advantage is

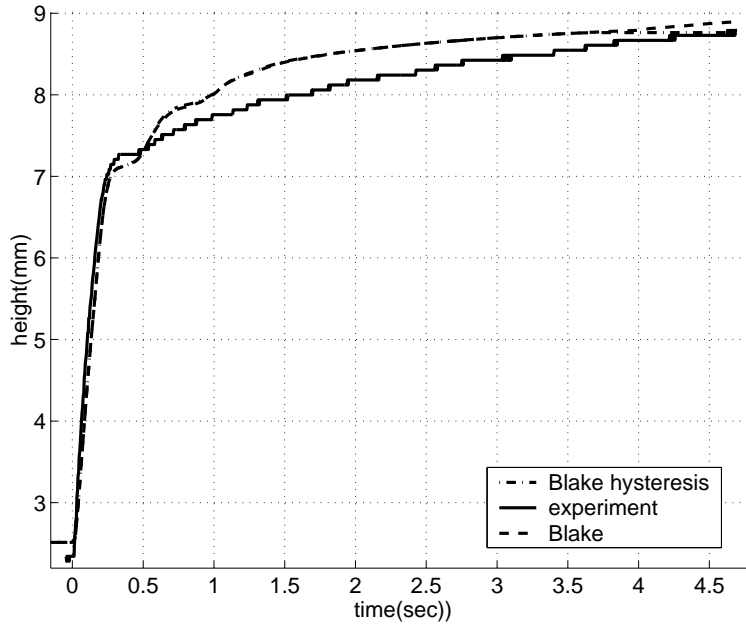


Figure 10.4: *Detra with Blake's model. Applying the same hysteresis as for M3 has not much effect.*

that this model is ready-to-use. Seeberg's model prescribes positive CLV accurately, and whenever the parameter in Blake's first order model is estimated with a reasonable accuracy, the behaviour of the negative CLV has some theoretical and empirical background. There is too little information about hysteresis effects to draw conclusions from the results with Detra and M3. In spite of the hopeful results, more research is needed in order to properly estimate a suitable hysteresis domain.

10.3 Future directions

More experimental validation is welcome to investigate the accuracy and the generality of the contact angle models and especially Blake's model. In particular it seems to be very useful to do more investigation about contact angle hysteresis. All tests were carried out in an axisymmetric tube with a straight wall and with one contact line. Conceptually, the extension to three-dimensional configurations with arbitrary boundaries and with an arbitrary number of contact lines is straightforward. Technically, this extension can be cumbersome. Some possible obstacles are outlined. The 3D extension of SAVOF96 is called ComFlo and approaches arbitrary liquid domains with cut (straight) boundary cells. The DCA is measured by means of the local liquid height and the contact line height on a Cartesian grid. Difficulties may arise numerically when the contact line moves along the sloped boundary or when the curvature/pressure in the liquid near the wall is influenced by the sloped boundary surface. Multiple contact lines are also hard to keep track of, section 9. The fact that in 2D the contact line is represented by one point and in 3D by multiple points should not give difficulties in case of one contact line, because the points are spatially well-defined (different points can be defined according to their location). Another obstacle to overcome is the direction in which

the contact line moves. In two dimensions the contact line moves only in two directions, up or down. In three dimensions, the liquid near the wall does not make just one contact angle, so a discretisation of the DCA and CLV has to be made for four different directions instead of two.

Acknowledgements

I wish to thank Dr. M. Dreyer and Dr. J. Gerstmann of the ZARM Institute of the University of Bremen for providing me their experimental results and for the useful discussions we had. I am also indebted to my fellow students who were always helpful and especially to Prof. Veldman for his many useful advices and for giving me all the liberty for my research.

Appendix A

Physics of Blake's model

Blake's model is based on the theory that at the contact line, molecular displacements take place between adsorption sites in the boundary. The frequency of these displacements and the distance between the adsorption sites determine the velocity at which the contact line moves. According to Eyring's theory of absolute reaction rates, at equilibrium ($\theta(t) = \theta_0$) the frequency of molecular displacements is related to the molar activation energy through

$$\kappa_w^0 = \frac{kT}{\hbar} \exp\left(\frac{-\Delta G_w^*}{NkT}\right) \quad (\text{A.1})$$

with the following parameters.

- κ_w^0 frequency of molecular displacements at equilibrium
- N Avogadro's number (6.02 mol^{-1})
- k Boltzmann's constant ($1.38 \cdot 10^{-23} \text{ J/K}$)
- \hbar Planck's constant ($6.63 \cdot 10^{-34} \text{ Js}$)
- ΔG_w^* molar activation free energy of wetting (J/mol)
- T temperature

And furthermore, $\kappa_w^0 = \kappa_w^+ = \kappa_w^-$, where

- κ_w^+ is the frequency of molecular displacements in forward direction, and
- κ_w^- is the frequency of molecular displacements in backward direction.

If some work w is added in forward direction, the frequencies become

$$\kappa_w^+ = \frac{kT}{\hbar} \exp\left(\frac{-\Delta G_w^*/N + w/2n}{kT}\right) \quad (\text{A.2})$$

$$\kappa_w^- = \frac{kT}{\hbar} \exp\left(\frac{-\Delta G_w^*/N - w/2n}{kT}\right) \quad (\text{A.3})$$

With n the number of adsorption sites per unit area
The net frequency becomes then

$$\kappa_w = \kappa_w^+ - \kappa_w^- = 2\kappa_w^0 \sinh\left(\frac{w}{2nkT}\right) \quad (\text{A.4})$$

The work in forward direction is done by the surface tension:

$$w = \gamma[\cos \theta_0 - \cos \theta(t)] \quad (\text{A.5})$$

The contact line velocity is interpreted as the net frequency of molecular displacements in forward direction (between adsorption sites) times the average distance between the adsorption sites λ .

$$h_t = \kappa_w \lambda = 2\lambda \kappa_w^0 \sinh\left(\frac{\gamma[\cos \theta_0 - \cos \theta(t)]}{2nkT}\right) \quad (\text{A.6})$$

This is the basic theory on which Blake has based his model. Further modifications of the parameters can be found in [26]. Eventually, the modifications lead to

$$h_t = 2\kappa_s^0 \lambda \frac{h}{\eta v} \sinh\left(\frac{\gamma[\cos \theta_0 - \cos \theta(t)]}{2nkT}\right) \quad (\text{A.7})$$

With $\kappa_s^0 = \kappa_w^0 \frac{\eta v}{h}$, where v is the molecular flow volume, which is equal to the volume of one molecule for 'simple' fluids.

Appendix B

Program description

The numerical model has been implemented in a FORTRAN program: SAVOF96. This appendix gives more detailed information about the calling sequence and the several variables and subroutines.

B.1 Calling sequence

The following scheme indicates the order in which the various subroutines are called. The main division is between the initialisation and the time loop. The loop involves post-processing routines. These post-processing routines are not necessary in the actual computation and will not be mentioned here. All choices concerning the performance of the program can be controlled by setting the right parameters in the input file **savof96-2.in**.

Initialisation	SETPAR	GRID		
	SETFLD	SURDEF		
		MKGEOM		
		RDGRID		
		LDSTAT		
		LABEL		
		BC	BCBND	
	Begin LOOP	INIT	BCBND	
		PETCAL		
		TILDE	BDYFRC	
SOLVEP		COEFF		
		CONVRT		
		PRESIT	SLAG	
		MILU		
		BC	BCBND	
		CFLCHK		
		DTADJ		
		VFCNV	LABEL	
		SVSTAT		

B.2 Subroutines

In this paragraph, the most important subroutines are listed. A short description of every subroutine listed is given.

BC	: sets the boundary conditions for the velocity components.
BCBND	: sets the boundary conditions at the outer boundary.
BDYFRC	: computes the apparent body force.
CFLCHK	: monitors the CFL-number and sets <code>flag</code> for time-step adjustment.
COEFF	: defines the coefficient matrix for the Poisson equation including the boundary conditions at the wall and the free surface.
CONVRT	: converts a 2-dim data structure into a 1-dim data structure for a more efficient implementation of the pressure solver.
DTADJ	: halves or doubles the time step (the old time step will be repeated).
GRID	: makes a (non-uniform) grid.
INIT	: starts a new time step.
LABEL	: labels empty, (preliminary) surface and full cells.
LDSTAT	: reads a restart file (produced by <code>SVSTAT</code>).
MILU	: solves the Poisson equation with the MILU algorithm.
MKGEOM	: defines the geometry.
PETCAL	: labels the surface cells and computes the pressure at the free surface with a local height function. Then the position of the free surface is calculated which will be used in <code>COEFF</code> to interpolate for the pressure boundary condition at the free surface.
PRESIT	: solves the Poisson equation and controls the SOR relaxation factor.
PRT	: prints and writes results.
RDGRID	: reads a 'broidery' file defining the geometry.
SETFLD	: initialises the fluid configuration.
SETPAR	: reads the input file.
SLAG	: performs one SOR sweep. It uses a 1-dimensional implementation.
SOLVEP	: organises the pressure calculation and updates the velocity.
SURDEF	: generates the liquid configuration.
SVSTAT	: writes a restart file.
TILDE	: integrates the momentum equations.
VFCONV	: moves the fluid, i.e. adjusts the VOF-function, and re-labels.

B.3 Common block variables

The globally used variables are defined within the common block structures in Fortran. The most important global variables are listed here. A short description is given for each variable.

/CASE/ contains the external body forces and their controls.

Ω , Del Ω : rotation rate, initial rotation relative to Ω .
X0, Y0 : in the case of 2D rotation: point about which the rotation takes place.
TwUp, TwDown : time to start and stop the rotation.
U0, V0 : initial velocity in x - and y -direction.
Ampl, Freq,
AAngle : amplitude, frequency and angle under which an oscillation is performed.
GX, GY : acceleration in x - and y -direction.
TxOn, TxOff,
TyOn, TyOff : times to turn the acceleration in x - and y -direction on and off.

/COEFP/ contains the coefficients for the pressure in the Poisson equation.

CC(I, J) : coefficient of $p_{i,j}$.
CN(I, J) : coefficient of $p_{i,j+1}$.
CS(I, J) : coefficient of $p_{i,j-1}$.
CE(I, J) : coefficient of $p_{i+1,j}$.
CW(I, J) : coefficient of $p_{i-1,j}$.
DIV(I, J) : right-hand side of the Poisson equation.

/GRIDAR/ contains the parameters involving the grid size.

X(I) : x -coordinates of the grid points.
XI(I) : x -coordinates of the cell centres.
DelX(I) : distance in the x -direction between 2 subsequent grid points ($\Delta x_i = x_i - x_{i-1}$).
Y(J) : y -coordinates of the grid points.
YJ(J) : y -coordinates of the cell centres.
DelY(J) : distance in the y -direction between 2 subsequent grid points ($\Delta y_j = y_j - y_{j-1}$).
RX(I), RXI(I),
RDX(I) : inverses of X(I), XI(I) and DelX(I).
RDY : inverse of DelY(J).
Circum(I) : circumference of a circle with radius XI(I) (in the axisymmetric case; 1 otherwise)
CYL, ICYL : floating-point and integer version of the 2D/axisymmetric switch (CYL=0 for 2D, CYL=1 for axisymmetric).
IMaxUs, JMaxUs,
IM1Us, JM1Us,
IM2Us, JM2Us : number of grid points in x - and y -direction
(IMaxUs=IM1Us+1=IM2Us+2,
JMaxUs=JM1Us+1=JM2Us+2).

/ORGA/ is used for cell labelling.

NF(I,J) : contains cell labels for the current time level.

NFN(I,J) : contains cell labels for the previous time level.

PETA(I,J) : coefficient used to interpolate the pressure.

For NF(I,J), all possible labels and their meanings are:

0 : full cell

1 : surface cell with a full cell to the left

2 : surface cell with a full cell to the right

3 : surface cell with a full cell at the bottom

4 : surface cell with a full cell at the top

5 : degenerated cell

6 : empty cell

7 : outflow cell

8 : inflow cell

9 : obstacle or boundary cell

/PHYS/ contains the pressure and velocities at the current and the previous time level respectively.

F(I,J) : VOF (volume of fluid)/indicator function.

U(I,J), UN(I,J) : horizontal/radial velocity.

V(I,J), VN(I,J) : vertical/axial velocity.

W(I,J), WN(I,J) : azimuthal velocity.

P(I,J), PN(I,J) : pressure.

PS(I,J) : pressure at the free surface.

VMAX : maximum attained velocity.

/TIMES/ contains parameters related to time levels and time steps.

Cycle : time step number.

T : current time.

DeIT : time step.

DeITMx : maximum allowed time step.

TFin : end time.

TStart : start time.

Appendix C

The input file

In this section we will discuss the main input file, called **savof96-2.in**. All the characteristics, numerically and physically, are set in this file. Also the information about post-processing must be set in this file. Furthermore the file contains a short explanation of many of the characteristics. Here an example of an input file is shown:

```
SAVOF96-2.0
**** tank geometry ****
icyl   Xmin   Xmax   Ymin   Ymax   SpGeom SpMot
1      0.0   0.015  0.0    0.08   0       0

**** liquid configuration ****
LiqCnf xp     yp     r      xq     yq
3      -0.01 -0.01  0.0    0.015  0.048

**** grid definition ****
iMaxUs jMaxUs cx     cy     Xpos   Ypos
60     60     0.0   0.0    0.0    0.0

**** liquid properties ****
Sigma  CAngle Nu
3.5E-5 5.5   2.56E-6

**** body forces and external motion: 2D ****
Gx     TxOn   TxOff  u0     Gy     TyOn   TyOff  v0
0.0    0.0    100    0.0    -980.0 0.0    1000.0 0.0
Ampl   Freq   Angle
0.0    0.0    90.0
Rpm    DelOme TwUp   TwDown x0     y0
0.0    0.0    0.0    100.0 0.0    0.0

**** body forces and external motion: axisymmetric ****
Gy     TyOn   TyOff  v0     Ampl   Freq
0.0    0.0    100.0 0.0    0.0    0.0
```

```

Rpm      DelOme  TwUp    TwDown
0.0      0.0      0.0     0.0

**** boundary conditions and inflow characteristics ****
left    right   top     bottom  UIn     VIn     Freqin  IPIN    PIn
1       1       1       2       0.0    0.0    0.0     0       0

**** upwind parameter and Poisson iteration parameters ****
Alpha   Epsi     ItMax   OmStrt  IMilu
1.0     1.0e-6   500     1.0     0

**** time step and restart control ****
TFin    DelT     CFLMax  PrtDt   svst    svdt
4.7     0.0001  0.5     0.02   0.5     0.5

**** print / plot control ****
gnu     avs     uvpf    velop   height  force
0       0       1       0       0       0

**** stream lines ****
nrx     nry     nrdt    xps     yps     xqs     yqs     t       dt/delt
0       0       0       135.0  30.0   150.0  50.0   0.0    4e4

**** fluxes ****
number of fluxes to be printed (flux01.out...flux##.out are created)
0
p1      p2      p3      hor

**** fill ratios ****
number of ratios to be printed (fill01.out...fill##.out are created)
0
xpf     ypf     xqf     yqf    (box with nodes (xpf,ypf) and (xqf,yqf))

-----
**** E X P L A N A T I O N **** E X P L A N A T I O N ****
-----

**TANK GEOMETRY**
icyl      : 0=2-dim; 1=axisymmetrical
SpGeom    : reads programmed geometry savof96.geo#
SpMot     : special motion

**LIQUID CONFIGURATION**
LiqCnf    : 1=lower part of cylinder with semi-circle - avg. height
           yp;
           2=toroide (drop) - mpt circle (xp,yp), radius r;
           3=rectangle - xp < x < xq and yp < y < yq;

```

4=drop along axis ($y=y_p$, r) falling in waterpool deep y_q ;
5=fluid filament - width r , height y_p +semi-sphere
7=empty bubble - radius r , center (x_p, y_p)

****GRID****

i_{MaxUs} (≤ 130), j_{MaxUs} (≤ 130): number of cells inclusive mirror cells
 cx , cy : stretchparameters - 0=no stretch; >0 =smaller cells near
position indicated by $x(y)$ pos; <0 =smaller cells away from
 $x(y)$ pos

****LIQUID PROPERTIES****

Σ : kinematic surface tension (σ/ρ)
 C_{Angle} : contact angle
 ν : kinematic viscosity (μ/ρ)

****EXTERNAL MOTION 2D****

G_x : acceleration in horizontal direction
 $T_{x\text{On}}, T_{x\text{Off}}$: timeinterval where acceleration G_x is active
($T_{x\text{On}} < t < T_{x\text{Off}}$)
 u_0 : horizontal initial velocity
 G_y : acceleration in vertical direction
 $T_{y\text{On}}, T_{y\text{Off}}$: timeinterval where acceleration G_y is active
($T_{y\text{On}} < t < T_{y\text{Off}}$)
 v_0 : vertical initial velocity
 $\text{Ampl}, \text{Freq}, \text{Angle}$: oscillation under angle with x-axis
 Rpm : rotation (per minute) in (x,y)-plane
 DelOme : relative initial rotation
 $T_{w\text{Up}}, T_{w\text{Down}}$: timeinterval where rotation is increased and decreased
 x_0, y_0 : center of rotation

****EXTERNAL MOTION AXISYMMETRIC****

G_y : acceleration in vertical direction
 $T_{y\text{On}}, T_{y\text{Off}}$: timeinterval where acceleration G_y is active
($T_{y\text{On}} < t < T_{y\text{Off}}$)
 v_0 : vertical initial velocity
 Ampl, Freq : oscillation in vertical direction
 Rpm : rotation (per minute)
 DelOme : relative initial rotation
 $T_{w\text{Up}}, T_{w\text{Down}}$: time interval where rotation is increased and decreased

[0 (spin-up) T_{up} (maximum) T_{down} (spin-down) $T_{\text{down}}+T_{\text{up}}$ (rest) T_{Fin}]

****BOUNDARY CONDITIONS****

bc : 1=slip; 2=no-slip; 7=outflow; 8=inflow
 $U_{\text{In}}, V_{\text{In}}, \text{FreqIn}$: inflow specification
 $I_{\text{Pin}}, P_{\text{In}}$: boundary and value of pressure condition

****NUMERICAL PARAMETERS****

Alpha : upwind parameter - 0=central; 1=upwind
Epsi : Poisson convergence criterion
ItMax : maximum number of iterations
OmStrt : initial relaxation factor

****TIME CONTROL****

TFin : endtime
Delt : timestep
CFLMax : maximum allowed CFL number
PrtDt : time between 2 small printouts
svst : save state for restart control
0= no restart backup;
1= saves restart file every svdt time-units;
2= starts with restart file, and proceeds like 1
svdt : time between saving of restart file

****PRINT/PLOT CONTROL****

uvpf : velocity and pressure data for visualisation with Matlab
gnu : interactive visualisation through Gnuplot
avs : velocity and pressure data in AVS format
velop : additional velocity and pressure output in 'savof96.out'
height : height of free surface at several moments in time
force : x- and y-components of force exerted by liquid

****STREAM LINES****

nrx : number of particles released in x-direction of
'start-matrix'
nry : number of particles released in y-direction of
'start-matrix'
nrtd : number of times that particles are released
xps,yps : left down corner of 'start-matrix'
xqs,yqs : right upper corner of 'start-matrix'
t : first release time of particles
dt/delt : time interval between releases

****FLUXES****

hor : 0=vertical line from (p3,p1) to (p3,p2)
1=horizontal line from (p1,p3) to (p2,p3)

****FILL RATIOS****

xpf,ypf : left down corner of fill box
xqf,yqf : right upper corner of fill box

Appendix D

Output files

SAVOF96 creates some output files automatically. These are files containing information about initialisation and progress in time. The files are named **savof96.out**, **grid.out**, **config.dat** and **diversen.res**. Other output files concern the post-processing and are only created when they are requested. A short description of some of the output files will be given now.

- **savof96.out**: This is SAVOF96's main output file. It contains among others the coordinates of the grid points, rough plots of the initial and final geometry and fluid configuration, the evolution of the time step, comments about the convergence and lines with the point in time, the number of iterations required to obtain the desired accuracy, the relative change in volume and an array representing the level of the fluid.
- **grid.out**: In this file, a rough representation of the initial geometry and fluid configuration is contained.
- **config.dat**: The dimensions of the calculation domain, the coordinates of the grid points and the initial labelling of the cells are contained in this file, which is also used for post-processing purposes.
- **diversen.res**: This file consists of lines with the evolution in time of several variables among which the time point, the volume of the fluid and the level of the fluid at the left side of the calculation domain in the middle of the calculation domain and at the right side of the calculation domain.
- **uvpf####.dat**: This file is used for post-processing in Matlab. It contains information about the velocities, pressure and liquid configuration.
- **uvpf.tim**: This file contains the number of **uvpf####.dat**-files made and the time points at which they are created.

Appendix E

Post-processing using Matlab

The results of the post-processing tasks that were set in the input file, can be viewed using the Matlab menu system. The powerful command `uicontrol` enables the creation of several menus, toggles, radio buttons and so on. The menu for viewing the obtained results is obtained by giving the command `liqdmnu`.

The `liqdmnu` menu is divided into several submenus (see figure E.1). Each of these submenus handles one post-processing aspect. The point-and-click system makes it not too hard for beginning users to process all information. Plots of most common combinations of variables can be drawn and printed. All variables are available for standard use in Matlab.



Figure E.1: The liqdmenu menu

Bibliography

- [1] S. van Mourik. Numerical modelling of the dynamic contact angle. A literary survey. 2002.
- [2] J. Gerrits. Fluid Flow in 3-D Complex Geometries-A Cartesian Grid Approach. Master's thesis, Rijksuniversiteit Groningen, 1996. Geometries. Master's thesis, Rijksuniversiteit Groningen, 1996.
- [3] T.D. Blake. Dynamic Contact Angles and Wetting Kinetics. In: '*Wettability*', p 251-309, 1993.
- [4] A.E.P. Veldman. Numerieke Stromingsleer. Lecture notes, Rijksuniversiteit Groningen, 1994.
- [5] K.M.T. Kleefsman. Numerical Simulation of Ship Motion Stabilisation by an Activated U-tube Anti-Roll Tank. Master's thesis, Rijksuniversiteit Groningen, 2000.
- [6] D-J. Kort. Numerical Study of Single Bubbles Rising in a Quiescent Fluid. Master's thesis, Rijksuniversiteit Groningen, 2001.
- [7] Testcase 3: Reorientation of a Liquid Surface after a Step Reduction of the Gravity.
- [8] J. Billingham. Mathematical Modelling of Moving Contact Lines. 1999.
- [9] J. Billingham. Nonlinear Sloshing in Zero Gravity. 2001.
- [10] Can a Dynamic Contact Angle Be Understood in Terms of a Friction Coefficient? A. Hamraoui et al. *J. Colloid Interface Science*, 226, 199-204, 2000.
- [11] C.W. Hirt and B.D. Nichols. Volume of Fluid (VOF) Method for the Dynamics of Free Boundaries. *J. Comput. Phys.*, 39, 1981.
- [12] S. Schiffer. A phenomenological model of dynamic contact angle. *Chem. Eng. Sc.*, 55, p 5933-5936, 2000.
- [13] G. Ström, M. Fredriksson and P. Stenius, *J. Coll. Inter. Sci* 134, p 117, 1990.
- [14] G. Ström, M. Fredriksson, P. Stenius and B. Radoev, *J. Coll. Inter. Sci* 134, p 107, 1990.
- [15] W. Hopf and Th. Geidel, *Coll. Polym. Sci.* 265, p 1075, 1987.
- [16] T.S. Jiang, S.G. Oh and J.C. Slattery. Correlation for dynamic contact angle. *J. Colloid Interface Sc.*, 69, 1, p 74-77, 1979.

- [17] M. Bracke, F. De Voeght and P.Joos. The kinetics of wetting: the dynamic contact angle. *Progr. Colloid Pol. Sc.*, 79, p 142-149, 1989.
- [18] J.E. Seeberg and J.C. Berg. Dynamic wetting in the flow of capillary number regime. *Chem. Eng. Sc.*, 47, p 4455-4464, 1992.
- [19] R. Burley and R.P.S. Jolly, *Chem. Eng. Sc.* 39, 1357, 1984.
- [20] H. Fan, Y.X. Gao, and X.Y. Huang. *Physics of Fluids* 13, p 1615, 2001.
- [21] W. Dörfler, O. Goncharova, and D. Kröner. Fluid Flow with Dynamic Contact Angle: Numerical Simulation *ZAMM* 82, 3, 167-176, 2002.
- [22] R. Golestanian and E. Raphaël, *Europhys. Lett.* 55, p 228-234, 2001.
- [23] D. Grubert and J.M. Yeomans, *Comp. Phys. Comm.* 121-122, p 236-239, 1999.
- [24] J.N. Tilton, *Chem. Eng. Sc.* 43, 1371, 1988.
- [25] G. B. Foote, A theoretical investigation of the dynamics of liquid drops. Ph. D. thesis, University of Arizona, 1971.
- [26] T.D. Blake. Dynamic Contact Angles and Wetting Kinetics. In: 'Wettability', p 251-309, 1993.
- [27] M. Dreyer, U. Schmid. Testcase 3: Reorientation of a Liquid Surface after a Step Reduction of the Gravity. In: experimental results of the COMPERE TEST CASES 1,2 and 3. November 2000.
- [28] C.W. Hirt and B.D. Nichols. Volume of Fluid (VOF) Method for the Dynamics of Free Boundaries. *J. Comput. Phys.*, 39, 1981.
- [29] B.V. Derjaguin, *C.R Acad. Sci. USSR* 51: 316, 1946.
- [30] R.J. Good, *J. Amer. Chem. Soc.* 75: 5041, 1952.
- [31] R.E. Johnson, Jr. and R.H. Dettre, in *Contact Angle, Wettability, and Adhesion*, Advances in Chemistry Series 43 (R.F. Gould, ed.), ACS, Washington, DC, 1964, p. 112; *J. Phys. Chem.* 68: 1744 (1964).
- [32] R.E. Johnson, Jr. and R.H. Dettre, in *Surface and Colloid Science*, Vol. 2 (E. Mateijevich, ed.), Wiley-Interscience, New York, 1969, pp 85-153.